

Simulations and Data Analysis for Air Force Optical Turbulence Forecasting Applications

**Joseph Werne
David Fritts
Thomas Lund**

**NorthWest Research Associates, Inc.
14508 NE 20th Street
Bellevue, WA 98007-3713**

Final Report

22 May 2007

APPROVED FOR PUBLIC RELEASE; DISTRIBUTION UNLIMITED.



**AIR FORCE RESEARCH LABORATORY
Space Vehicles Directorate
29 Randolph Road
AIR FORCE MATERIEL COMMAND
Hanscom AFB, MA 01731-3010**

NOTICES

Using Government drawings, specifications, or other data included in this document for any purpose other than Government procurement does not in any way obligate the U.S. Government. The fact that the Government formulated or supplied the drawings, specifications, or other data does not license the holder or any other person or corporation; or convey any rights or permission to manufacture, use, or sell any patented invention that may relate to them.

This report was cleared for public release and is available to the general public, including foreign nationals. Qualified requestors may obtain additional copies from the Defense Technical Information Center (DTIC) (<http://www.dtic.mil>). All others should apply to the National Technical Information Service.

AFRL-VS-HA-TR-2007-1059 HAS BEEN REVIEWED AND IS APPROVED FOR PUBLICATION IN ACCORDANCE WITH ASSIGNED DISTRIBUTION STATEMENT.

//Signature//

FRANK RUGGIERO
Contract Manager

//Signature//

BRIAN GRIFFITH, Maj, USAF, Chief
Battlespace Surveillance Innovation Center

This report is published in the interest of scientific and technical information exchange, and its publication does not constitute the Government's approval or disapproval of its ideas or findings.

REPORT DOCUMENTATION PAGEForm Approved
OMB No. 0704-0188

Public reporting burden for this collection of information is estimated to average 1 hour per response, including the time for reviewing instructions, searching existing data sources, gathering and maintaining the data needed, and completing and reviewing this collection of information. Send comments regarding this burden estimate or any other aspect of this collection of information, including suggestions for reducing this burden to Department of Defense, Washington Headquarters Services, Directorate for Information Operations and Reports (0704-0188), 1215 Jefferson Davis Highway, Suite 1204, Arlington, VA 22202-4302. Respondents should be aware that notwithstanding any other provision of law, no person shall be subject to any penalty for failing to comply with a collection of information if it does not display a currently valid OMB control number. PLEASE DO NOT RETURN YOUR FORM TO THE ABOVE ADDRESS.

1. REPORT DATE (DD-MM-YYYY) 22-05-2007		2. REPORT TYPE Final Report		3. DATES COVERED (From - To) 26/07/2002 - 25/07/2006	
4. TITLE AND SUBTITLE Simulations and Data Analysis for Air Force Optical Turbulence Forecasting Applications				5a. CONTRACT NUMBER F19628-02-C-0037	
				5b. GRANT NUMBER N/A	
				5c. PROGRAM ELEMENT NUMBER N/A	
6. AUTHOR(S) J. Werne, D.C. Fritts, and T. Lund				5d. PROJECT NUMBER 1010	
				5e. TASK NUMBER OT	
				5f. WORK UNIT NUMBER A1	
7. PERFORMING ORGANIZATION NAME(S) AND ADDRESS(ES) NorthWest Research Associates, Inc. 14508 NE 20 th Street Bellevue, WA 98007-3713				8. PERFORMING ORGANIZATION REPORT NUMBER NWRA-CoRA-07-R360	
9. SPONSORING / MONITORING AGENCY NAME(S) AND ADDRESS(ES) Air Force Research Laboratory 29 Randolph Road Hanscom AFB, MA 01731-3010				10. SPONSOR/MONITOR'S ACRONYM(S) AFRL/VSBYA	
				11. SPONSOR/MONITOR'S REPORT NUMBER(S) AFRL-VS-HATR-2007-1059	
12. DISTRIBUTION / AVAILABILITY STATEMENT Approved for Public Release; Distribution unlimited.					
13. SUPPLEMENTARY NOTES					
14. ABSTRACT We completed a series of Direct-Numerical and Large-Eddy Simulations (DNS and LES) of wind-shear instability and gravity wave breaking and associated analysis to characterize atmospheric turbulence and its optical impacts. We also analyzed hundreds of rawinsonde profiles to determine the parameters associated with turbulence layers observed in the troposphere and stratosphere. Finally, we developed a Bayesian Hierarchical Modeling (BHM) framework for combining the simulation and observational results so that atmospheric turbulence and optical turbulence atmospheric decision aids can be developed and improved. These results can also be used to develop subgrid-scale turbulence and optical turbulence parameterizations for operational mesoscale Numerical Weather Prediction models, e.g., the Weather Research and Forecasting Model (WRF).					
15. SUBJECT TERMS Direct Numerical Simulation, Large-Eddy Simulation, Bayesian Hierarchical Modeling					
16. SECURITY CLASSIFICATION OF:			17. LIMITATION OF ABSTRACT SAR	18. NUMBER OF PAGES 72	19a. NAME OF RESPONSIBLE PERSON Frank Ruggiero
a. REPORT UNCLASSIFIED	b. ABSTRACT UNCLASSIFIED	c. THIS PAGE UNCLASSIFIED			19b. TELEPHONE NUMBER (include area code) 781-377-2940

Table of Contents

1.	INTRODUCTION	1
2.	BACKGROUND	1
3.	TECHNICAL APPROACH.....	2
3.1.	High-Resolution Simulation Techniques.....	3
3.1.1.	TRIPLE Optimization Details.....	4
3.1.2.	TRIPLE Job-Preparation and Automation Scripts.....	5
3.1.3.	Technical and Computational Challenges	6
3.1.4.	DNS/LES Data Analysis.....	6
3.2.	Analysis of Observational Data	7
3.2.1.	Rawinsonde Data	7
3.2.2.	Aircraft Data	8
3.3.	Probabilistic Modeling.....	8
3.3.1.	Bayesian Hierarchical Modeling.....	9
4.	RESULTS AND DISCUSSION	9
4.1.	DNS/LES Solutions	10
4.1.1.	Numerical-Solution Validation.....	10
4.1.2.	Wind-Shear Simulations	12
4.1.3.	Gravity-Wave-Breaking Simulations.....	17
4.1.4.	Implications of DNS Simulations for C_n^2 and SGS Modeling ..	18
4.1.5.	LES Solutions and Turbulence Modeling.....	19
4.2.	Atmospheric Data Analysis	21
4.2.1.	Balloon-Data Analysis	21
4.2.2.	Aircraft-Data Analysis	22
4.2.3.	BHM Approach to Probabilistic Prediction.....	23
4.2.4.	Intrinsic Limitations of Deterministic NWP Modeling	25
	REFERENCES.....	58

Figures

Figure 1. <i>Parallel performance on five supercomputer platforms</i>	27
Figure 2. <i>Vorticity in stratified wind shear for $Ri=0.15$ showing large range of length scales present.</i>	27
Figure 3. <i>Temperature in stratified wind shear for $Ri=0.05$ and $Re=2500$ at seven distinct times during the flow evolution.</i>	28
Figure 4. <i>Temperature in stratified wind shear for $Ri=0.10$ and $Re=2500$.</i>	30
Figure 5. <i>Temperature in stratified wind shear for $Ri=0.15$ and $Re=2900$.</i>	32
Figure 6. <i>Temperature in stratified wind shear for $Ri=0.20$ and $Re=4000$.</i>	34
Figure 7. <i>Vorticity magnitude in stratified wind shear for $Ri=0.05$ and $Re=2500$.</i>	36
Figure 8. <i>Vorticity magnitude in stratified wind shear for $Ri=0.10$ and $Re=2500$.</i>	38
Figure 9. <i>Vorticity magnitude in stratified wind shear for $Ri=0.15$ and $Re=2900$.</i>	40
Figure 10. <i>Vorticity magnitude in stratified wind shear for $Ri=0.20$ and $Re=4000$.</i>	42
Figure 11. <i>Time evolution of fluctuation kinetic energy KE (solid line) and an estimate for the potential energy PE (dashed line) (top panels) and the maximum of each vorticity component (bottom panels) for (a) $Ri=0.05$, (b) $Ri=0.10$, (c) $Ri=0.15$, and (d) $Ri=0.20$.</i>	44
Figure 12. <i>$Ri=0.05$ – Horizontally averaged profiles for the mean temperature (upper left) and mean streamwise velocity (lower left) and for the normalized temperature variance (upper middle) and normalized velocity variance (lower middle).</i>	45
Figure 13. <i>$Ri=0.20$ – Horizontally averaged profiles for the mean temperature (upper left) and mean streamwise velocity (lower left) and for the normalized temperature variance (upper middle) and normalized velocity variance (lower middle).</i>	45
Figure 14. <i>$Ri(z)$ profiles for wind-shear simulations with $Ri=0.20$ (left) and $Ri=0.05$ (right). Initial (dotted) and final (solid) profiles are shown. The time of the final profile is selected at late time during final restratification.</i>	46
Figure 15. <i>Mid-layer Richardson number $Ri(0)$ (left panel) and N/S (right panel) versus Nt for $Ri=0.05$ (dashed) and $Ri=0.20$ (solid).</i>	46
Figure 16. <i>Final layer depth L versus initial layer Richardson number Ri for four wind-shear simulations</i>	47
Figure 17. <i>3D evolution of vortex tubes (λ_2 visualization) for an amplitude $A=1.1$ gravity wave viewed from the side and from above.</i>	48
Figure 18. <i>3D evolution of vortex tubes (λ_2 visualization) for an amplitude $A=0.9$ gravity wave viewed from the side and from above.</i>	49
Figure 19. <i>3D volume rendering of the thermal (blue) and viscous (orange) dissipation for a wind-shear simulation with $Ri=0.05$.</i>	50

Figure 20. <i>DNS/LES comparisons of wind-shear simulations with $Ri=0.05$ and $Re=2500$.</i>	51
Figure 21. <i>Structure-function-fit parameters versus height for LES (blue) and DNS (red) solutions.</i>	52
Figure 22. <i>Probability density functions for atmospheric shear layers derived from 440 rawinsonde flights over Kansas and Utah.</i>	53
Figure 23. <i>Same as Figure 22, but all PDFs are with respect to the reduced variables $X'=(X-\langle X \rangle)/X_{RMS}$, where X represents one of the variables plotted in Figure 22, and $\langle X \rangle$ and X_{RMS} are the average and RMS values of X respectively.</i>	54
Figure 24. <i>Cliff-ramp structures in aircraft measurements (left) and DNS wind-shear solutions (right).</i>	55
Figure 25. <i>Left panel: VTMX Wheeler Farm rawinsonde data, 17 Oct 2000, 0:48 UTC.</i>	56
Figure 26. <i>Mean and RMS of the ensemble PDF's shown in Figure 25.</i>	57

Preface

The numerical simulations in this report were conducted using Department of Defense (DoD) supercomputer time provided through several Challenge Allocations awarded by the High Performance Computing Modernization Office (HPCMO). Systems at the U.S. Engineer Research and Development Center (ERDC) and the Naval Oceanographic Office (NAVO) were used. The rawinsonde data analyzed was obtained through our participation in the CASES-99 and VTMX field programs, sponsored by the National Science Foundation (NSF) and the Department of Energy (DOE). Additional Air Force rawinsonde data were provided by Dr. Frank Ruggiero of the Air Force Research Laboratory (AFRL). The comparisons with aircraft data were made possible by results and analysis provided by Dr. Donald Wroblewski of Boston University (BU). Some of the simulations and visualization work was done by Drs. Ling Wang, Kam Wan, Chris Bizon, Chris Meyer, and Ms. Melissa Davis-Mansour.

1. INTRODUCTION

In the summer of 2002, NorthWest Research Associates, Inc. (NWRA) was awarded a three-year contract by the Air Force Research Laboratory (AFRL) for a proposal submitted to the High-Energy Laser – Joint Tactical Office (HEL-JTO) program to perform the research and development needed to develop and improve reliable Atmospheric Decision Aids (ADAs) for Air Force optical turbulence forecasting applications and operational support. Example applications include laser-weapons and laser-communication systems.

Though the HEL-JTO program was unexpectedly terminated less than one year after project initiation, AFRL continued to sponsor this effort under the original contract, extending the period of performance by 2.5 years and fully funding the original contract amount. We are grateful that AFRL managed to keep this effort alive which made the research presented here possible.

During this project, we completed a series of Direct-Numerical and Large-Eddy Simulations (DNS and LES) of relevant atmospheric dynamical processes occurring in the troposphere and stratosphere (e.g., wind-shear instability and gravity wave breaking), and analyzed the statistics of the resulting atmospheric turbulence. Two DoD High Performance Computing Modernization Program (HPCMP) Challenge Allocations at two Major Shared Resource Centers (MSRCs), i.e., ERDC and NAVO, were awarded to us to carry out this part of the work. We also analyzed hundreds of rawinsonde profiles in order to determine the parameters associated with turbulence layers observed in the troposphere and stratosphere. This data was obtained through our participation in the CASES-99 and VTMX field campaigns, as well as Air Force rawinsonde data provided by Dr. Frank Ruggiero. Finally, we developed a Bayesian Hierarchical Modeling (BHM) framework for combining the simulation and observational results so that they may be used to develop and/or improve atmospheric turbulence and optical turbulence ADAs. This approach and data can also be used to develop subgrid-scale turbulence and optical turbulence parameterizations for operational mesoscale Numerical Weather Prediction (NWP) models, e.g., the Weather Research and Forecasting Model (WRF).

2. BACKGROUND

At the outset of this project, the Air Force was developing an ADA to provide optical turbulence predictions in support of the Airborne Laser (ABL). The starting point for the ABL ADA was the following model of the index-of-refraction second-order structure constant C_n^2 :

$$C_n^2 = a \left(\frac{K_n}{K_M} \right) \ell_o^{4/3} (\partial_z \bar{n})^2, \quad (1)$$

where $a=2.8$ is a universal constant; K_M and K_n are eddy diffusion coefficients for momentum and the index of refraction n ; $\partial_z \bar{n}$ is the mean vertical gradient of n ; and ℓ_o is the “outer length scale” for turbulent motion, above which effects of stratification are felt.

Dewan (1980) and others argue that ℓ_o is of order and $\ell_o \approx 0.1 L$, where L is the depth of a turbulent mixing layer. Equation (1) was proposed by Tatarski in 1961 (Tatarski 1961); a detailed description of its derivation is given in Dewan (1980). The critical three assumptions made when deriving (1) are: 1) stationary turbulence, in which production balances dissipation (i.e., $P \approx \varepsilon$) for both n and momentum; 2) homogeneous turbulence, for which all turbulent diffusion terms play a minor role and do not influence the dominant balance of $P \approx \varepsilon$; and 3) Prandtl mixing-length arguments, for which transport and mixing are described by an eddy viscosity and down-gradient fluxes. All of the quantities in (1) can be either estimated or deduced from mesoscale-model output, except for ℓ_o , which Dewan et al. (1993) estimate from filtered wind profiles. They use a filter width of 300m, i.e., the same resolution as archived radiosonde data and also the resolution of the Air Force Weather Agency (AFWA) mesoscale model at ABL operational altitudes, to produce a linear fit of Y versus S_{raw} , where S_{raw} is the filtered shear rate and $10^Y = \langle L^{4/3} \rangle$. The large scatter in the data (see Figures 2 and 3 of Dewan et al. 1993) indicates that L correlates poorly with the filtered shear rate S_{raw} , and that the uncertainty in Y is as large as ± 1 . This translates to an uncertainty in C_n^2 that spans as much as a factor of 100, which is as large as (and in some cases larger than!) the natural variation of C_n^2 exhibited by thermosonde data (Coulman et al. 1995). As a result, (1) does not predict C_n^2 with any greater fidelity than a compiled C_n^2 climatology, e.g., CLEAR-1 (Beland 1993).

The reasons for the inability of (1) to provide greater predictive skill lies in a) the coarseness of (1) as a model for stratified turbulence and b) the absence of more detailed physics in the regression relating L and S_{raw} . For example, local maxima in C_n^2 occur at the edges of stratified mixing layers (Gibson-Wilde et al. 2000, Werne and Fritts 2001, Pettersson-Reif et al. 2002). These regions define the boundaries between vigorous turbulence in the middle of the layers and the laminar motions outside. Based on recent research (see §4), we know these regions to be nonstationary, inhomogeneous, and anisotropic (Werne and Fritts 2000, 2001). And from simulation work done as a part of this project, we also know that turbulent diffusion, counter-gradient fluxes, and anomalous pressure-strain correlations are all significant here as well (Pettersson-Reif et al. 2002, Werne et al. 2005). Hence, all three of the assumptions used to derive (1) are violated in the regions that are most important for evaluating C_n^2 . It is clear that a more quantitative description of C_n^2 than (1) is required if reliable forecasts are to be made.

3. TECHNICAL APPROACH

During the course of this work, we pursued three distinct project components: 1) high-resolution numerical simulations; 2) rawinsonde and aircraft data analysis; and 3) the development of a new probabilistic modeling approach, which can be used both for C_n^2 modeling and as the basis for a new SGS parameterization method for real-time mesoscale forecasting. Below, we separately describe the technical approach used for each of these components.

3.1. High-Resolution Simulation Techniques

The technical approach employed for the high-resolution simulations of atmospheric wind shears and gravity wave breaking used both DNS and LES techniques. The DNS code, named TRIPLE, is an incompressible pseudo-spectral Navier-Stokes solver that uses Fourier and Chebyshev spatial discretizations. It is a mature production code that has served as the workhorse for six DoD HPCMP and NSF Grand Challenge projects and two HPCMP Capability Applications Projects (CAP) Phase II projects at seven different supercomputer centers (ERDC, NAVO, ARL, ASC, AHPCRC, PSC, and SDSC)¹ on ten different MPP platforms (Cray T3D, T3E, XT3, IBM P3, P4+, P5+, SGI O2K, O3K, Onyx, Compaq SC40/45). The numerical method advances the Fourier and/or Chebyshev coefficients in spectral space. Potential truncation errors are removed using the “tau”-correction (Kleisser and Schumann 1980, Werne 1995, 1998), and vertical stacking of Chebyshev domains is possible. The method is Nth-order accurate in space, where N is the number of spectral modes. Depending on the application (i.e., wave-breaking, shear, convection, etc.), different spatial representations are used. Possible boundary conditions include stress-free, no-slip, fixed-temperature or heat-flux, radiative, incident gravity waves, or any combination thereof. For shear-instability and reduced-equation studies, greater computation speeds are achieved by employing simpler boundary conditions permitted by these problems. For these cases, stress-free top and bottom boundaries permit Fourier representations in the vertical, and complicated inversion operations can be avoided.

Time-stepping is conducted using the mixed implicit/explicit 3rd-order Runge-Kutta (RK3) scheme of Spalart et al. (1991), which has the same storage requirements of most 2nd-order schemes, allowing us to achieve larger numerical domains than would otherwise be possible. Nonlinear terms are treated explicitly, while buoyancy and diffusion are handled implicitly. Derivatives (nonlinear terms) are computed efficiently in spectral (physical) space.

The majority of the LES work done on this project was accomplished using an updated version of Dr. Peter Sullivan’s Planetary Boundary Layer (PBL) code. Dr. Sullivan was a consultant on this project. Sullivan’s LES code has been successfully applied to a wide range of problems in both atmospheric and oceanic planetary boundary layers. The solution algorithm is a mixed pseudo-spectral/finite-difference collocation scheme. Vertical derivatives are approximated with 2nd-order centered differencing. Horizontal velocity components, virtual potential temperature, and pressure are stored at co-located grid locations staggered vertically from the vertical velocity and SGS energy. Time integration uses an explicit 3rd-order Runge-Kutta scheme for all terms except pressure. A fractional-step method is used to determine the pressure at each Runge-Kutta substep. The pressure satisfies a Poisson equation, which is solved using Fourier methods

¹ ARL is the Army Research Laboratory; ASC is the Aeronautical Systems Center; AHPCRC is the Army High Performance Computing Research Center; PSC is the Pittsburgh Supercomputing Center; SDSC is the San Diego Supercomputing Center. ERDC, NAVO, and ASC are DoD Major Share Resource Centers (MSRCs).

and the inversion of a tri-diagonal matrix. The code is written in MPI and has been in production on IBM SP and Cray platforms at NAVO and ERDC. For current studies, SGS turbulence is modeled using either a two-part eddy-viscosity model (Sullivan et al. 1994) requiring the solution of a transport equation for SGS energy or a dynamic SGS procedure which uses either the two-part procedure or a traditional eddy-viscosity model (e.g., Smagorinsky 1963) and a gradient-diffusion eddy-diffusivity model. Alternate SGS prescriptions can be accommodated in a straightforward fashion. Horizontal boundary conditions are periodic. The upper and lower boundaries may be periodic, stress free, or radiate gravity waves. Other vertical boundary conditions can be implemented easily. A novel feature of the present LES code is the ability to nest high-resolution meshes within the larger outer domain (Sullivan et al. 1996). Two-way communication between nested and outer grids utilizes spectral interpolation and Germano's identity (Germano et al. 1991), which enforces total-flux conservation on the different meshes.

In order to isolate the LES SGS model during testing and comparisons with the DNS solutions, in the last year of this project we converted TRIPLE from a DNS-only code to a DNS/LES code, which could include the SGS schemes in Dr. Sullivan's PBL code by setting an LES parameter in TRIPLE's job-preparation input file.

3.1.1. TRIPLE Optimization Details

Three-dimensional Fast Fourier Transforms (FFTs) comprise 75% of TRIPLE's cost, and care is therefore taken to ensure they are performed efficiently. Operation counts are reduced by exploiting the symmetry properties of real FFTs, and loop-level optimization and temporary storage are used to maximize cache reuse, e.g., trigonometric multi-angle recurrence relations replace traditional table-look-up algorithms, and higher radix routines (e.g., powers of 2, 3, 4, and 5) are separately coded. Finally, transposes are used to ensure FFTs are only conducted in the contiguous array direction.

Inter-processor communication is dominated by global transposes needed for the 3D FFTs. This involves an all-to-all communication pattern that minimizes latency and maximizes message size. Such communication can be challenging for large distributed memory systems and must be coded carefully. It also requires a fast inter-node network.

Extremely high parallel efficiency is achieved with TRIPLE by minimizing serial operations, conducting efficient parallel I/O using hierarchical data structuring and write-behind data buffering (Werne, et al. 2000), and using fast communication calls, available either via SHMEM or MPI library routines. Figure 1 shows parallel scaling tests using a fixed per-processor problem size on five different platforms. The variable plotted, C , is proportional to the wall-clock time per compute cycle. Fluctuations in the data with NCPU result from the cache-reuse characteristics of the different radix FFT routines for different problem shapes. In the left panel, C is multiplied by the peak FLOP rate S of the processor used so that the communication characteristics of the different platforms

can be isolated.² In the right panel, C alone is plotted, revealing the relative wall-clock time needed to complete a simulation on the platforms for which we are requesting Challenge time (P5+ and XT3). P4+ data is also included in the right panel so that the P4+ and P5+ can be directly compared. Of the platforms tested, the Cray XT3 exhibits the best asymptotic performance with 100% parallelization efficiency (i.e., $C \cdot S$ is constant within the fluctuations in the data). The Cray T3E, IBM P4+, and IBM P5+ exhibit similar parallel performance, with an efficiency of 99.976% according to Amdahl's Law or $m=95\%$ when evaluating the grind time.³ The P4+ exhibits slightly better parallel performance than the P5+ because the inter-node network for the two machines is basically the same, while the P5+ has twice as many processors per node and its processor is 11.8% faster.⁴ The Xeon cluster exhibits the worst performance (99.89% Amdahl's Law or $m=88\%$ for the grind time).

The XT3's superior performance is due to its excellent network – 7.6 GB/s inter-node bandwidth and 5.4-6.6 μ s latency. The T3E and P4+/P5+ have bandwidths of 420 and 450 MB/s and latencies of 5.6-8.2 and 2-3 μ s, respectively. The ratio of the per-processor bandwidth to the per-processor FLOP rate is 0.066, 0.35, and 1.46 B/flop for the P4+, T3E, and XT3, revealing why the XT3 is advantageous for TRIPLE's all-to-all communication pattern. Nevertheless, the parallel efficiency for the T3E and the P4+/P5+ is more than adequate for our needs. Once the faster processor speed S and heterogeneous network of the P5+ is factored in, overall the P5+ is only 10% slower than the XT3 for certain “sweet spot” values of the grid size and NCPUs (e.g., NCPUs=900, 1200 and 1600; see right panel). We take advantage of this behavior when conducting simulations on the P5+ by carefully choosing value of NCPUs. In contrast to these systems, the Xeon cluster performance was determined to be unacceptable for TRIPLE. The inter-node bandwidth per processor on this system was only 250 MB/s, and the latency was 19 μ s when both processors per node are used. As a result, the computational cost grew too rapidly with NCPUs to be a useful platform for TRIPLE.

3.1.2. TRIPLE Job-Preparation and Automation Scripts

Significant logistical problems arise from many of the supporting operations associated with large-scale computing. We have addressed these challenges by developing a modular system of code and Perl scripts to simplify, streamline, and automate large-scale computing tasks. Strategies include: 1) automating job preparation and submission; 2) defining an irreducible set of job-related parameters for the job-input file so that redundancy is removed during batch-job specification (and user error thereby minimized); 3) automatically migrating large 3D data volumes to archival storage in real

² If no time were spent in communication, $C \cdot S$ would equal the operation count per mode per time step per processor, and all data in the left panel would be identical (and flat). Separate curves result from differences in the way communication is managed by the different platforms.

³ Grind time g_n is defined by $g_n = g_1/n^m$, where g_1 is the time required for a calculation on one processor, and g_n is the time used on n processors. Parallel efficiency is given by m .

⁴ On average, TRIPLE is 3.6% faster on the P5+ than on the P4+. This is apparent in the right panel of Figure 1 where C is not normalized by the processor speed S .

time so that impact on local supercomputer disk space is minimized; and 4) developing a translation layer for predictable tasks so that code can be more easily maintained at multiple centers and users need not memorize multiple syntaxes to solve the same problem; these tasks include file transfer operations, queue-system control directives and parameters, and job-submission syntax. This last set of tools (item 4) forms the core of the Uniform Command Line Interface (UCLI); see www.pstoolkit.org, home of the Practical Supercomputer Toolkit. With this suite of software tools, users on this project were able to avoid many repetitive and mundane tasks, and instead were able to concentrate on higher-level scientific tasks.

3.1.3. Technical and Computational Challenges

The challenges for the simulations proposed arise from the anisotropic and episodic nature of stratospheric turbulence and the enormous range of length scales it possesses; see Figure 2. The wind-shear and wave-breaking processes 1) develop from flow instabilities, 2) progress through a high-Re laminar state before 3) becoming fully turbulent, 4) subsiding as turbulence decays, and 5) the flow restratifies (Werne et al. 2005). Though a properly specified SGS model can be useful in mitigating the enormous cost of stage 3 in this scenario, it cannot address the similarly daunting resolution requirements that accompany stage 2, and though it might be able to handle stage 4, care must be taken at late time as the spectral gap closes between the energy-containing and dissipation ranges in the spectrum and the SGS-model assumptions are violated. When the SGS model loses validity, DNS is the only available option, and it demands large computational resources; e.g., computer memory and cost scale as $Re^{9/4}$ and Re^3 , respectively. This is prohibitive when one considers stratospheric Reynolds numbers of 10^7 - 10^8 . In contrast, current DNS of stratified turbulence reach values of only $Re \approx 10^5$. Though still expensive, thankfully these Reynolds numbers are sufficient (barely) to access the asymptotic range of turbulence at high Re, and direct comparisons with atmospheric observations demonstrate their relevance (Werne and Fritts 2000). Until we discover how to exploit ways to overcome the inherent difficulties presented by stage 2 and, to a lesser degree, stage 4, expensive DNS calculations will continue to be necessary when studying episodic atmospheric turbulent phenomena.

3.1.4. DNS/LES Data Analysis

The DNS and LES results were analyzed in number of ways. First, flow visualization was conducted to determine the basic flow morphology and dynamics. Next, an exhaustive statistical analysis package was developed to quantify turbulence budgets and other quantities of interest. These included spanwise and full-horizontal averaged terms in the evolution of all of the Reynolds-stress components $u_i u_j$, the turbulent heat flux $u_i \theta$, the dissipation tensors $\nabla u_i \bullet \nabla u_j$ and $\nabla \theta \bullet \nabla \theta$, as well as other quantities (e.g., 2nd-order structure constants for all flow fields, anisotropy invariants II and III, and more. Here u_i is the i^{th} component of the fluctuating velocity field and θ is the fluctuating potential temperature. Results were compared with published atmospheric measurements and with data from field campaigns designed to look at stably stratified atmospheric dynamics.

DNS and LES results were compared to evaluate the skill of the SGS model in reproducing the DNS solutions.

3.2. Analysis of Observational Data

Observational data were analyzed to better understand atmospheric dynamics that give rise to optical turbulence in the upper troposphere and lower stratosphere and to validate the DNS results. High-resolution rawinsonde data from the CASES-99 and VTMX field campaigns were used to evaluate the properties of turbulent layers observed in the atmosphere, while aircraft data collected using three NOAA BAT probes aboard the Grob G520T Egrett were used to compare in detail with the simulation results. The Egrett data was also used to deduce shear-turbulence characteristics in the edges of jet streams over England and Australia.

3.2.1. Rawinsonde Data

The rawinsonde data analyzed were collected at 4 sites (Smileyberg, Leon, Beaumont, and Eldorado) in Kansas during October 1999 and at 3 sites (Wheeler Farm, Jordan Narrows, and the Salt Lake City Airport) in Utah's Great Salt Lake Basin during October 2000. In total, data from 440 sonde flights were analyzed. Measurement profiles collected included atmospheric pressure, temperature, relative humidity, GPS location, and wind speed and direction at typically a few meters vertical resolution. The maximum altitude attained varied from flight to flight, with the highest flights reaching up to 28 km.

In order to determine observed turbulent-layer properties from the rawinsonde data, the following procedure was employed. First, quality control of the data files was done, and bad data were identified. Second, where possible, linear interpolation was used to estimate bad-data values for altitude and pressure. Third, cubic-spline interpolation was used to interpolate the raw data to a uniform grid with a vertical resolution set to the minimum vertical spacing reported in the raw data file; the resolution was reduced if more than 40,000 vertical levels resulted from this procedure. The resulting interpolated data possessed resolutions of order $O(1\text{m})$. Care was taken to address the finite bit-resolution of the measurements by identifying instrument threshold values for over-sampled data. Without this step, many false turbulent layers would be reported. Vertical derivatives were then taken using 3-point Lagrangian differentiation.

From the processed rawinsonde data, we identified atmospheric shear layers, and we computed parameters of interest, such as the layer's altitude Z , depth L , velocity jump ΔU , potential temperature drop ΔT , turning-shear ratio V_0/U_0 (defined below), etc., and derived quantities, such as the layer Reynolds number $Re_L = \Delta U L / \nu$ and bulk Richardson number $Ri_L = g\alpha\Delta T L / (\Delta U)^2$. Here, g , ν and α are the acceleration due to gravity, the kinematic viscosity, and the thermal expansion coefficient in the atmosphere. Layers were identified by first locating local maxima in $\partial_z \mathbf{U} \cdot \partial_z \mathbf{U}$, where \mathbf{U} is the horizontal wind vector and ∂_z is the vertical derivative. Adjacent local minima (above and below the

computed mid-layer maxima) or zero-crossings of the shear in the direction of maximum mid-layer shear were then used to define the layer edges.

We also evaluated the degree to which one might deduce the actual atmospheric Richardson-number profile given a simulated profile predicted by a model. To do this we needed to smooth the rawinsonde data to successively coarser resolutions before analyzing the results. This was carried out on the interpolated data by smoothing to 11-, 33-, 100-, and 300-m vertical resolutions using box-car averaging.

The Interactive Data Language (IDL) software package from Research Systems, Inc., was used for the rawinsonde data analysis.

3.2.2. Aircraft Data

Aircraft data were collected by Dr. George Hacker and colleagues using Airborne Research Australia's high-altitude Grob G520T Egrett. Measurements were taken at altitudes up to 15 km at a mean airspeed of 100 m/s and with a maximum flight duration of up to 8 hours. Three NOAA BAT probes were located under the wings and high on the tail. They reported temperature and all three wind components at 50 Hz. The data were analyzed by Drs. Don Wroblewski (Boston University) and Owen Cote (AFRL).

Regions of interest in the aircraft data were initially identified by noting significant vertical velocity fluctuations above the background fluctuations of about 0.3 m/s. The data were low-pass filtered, and second-order structure constants for all measured quantities were evaluated. Also, properties of cliff-ramp structures observed in the data were quantified, and results from the measurements were compared with the DNS results described above.

By examining the data in this way, only a portion of the data has been processed and analyzed to date.

3.3. Probabilistic Modeling

An unanticipated development at the outset of this work was the ability to combine our DNS/LES results with observational data to produce hybrid deterministic/probabilistic C_n^2 and SGS models, which can forecast both statistical expectation values and model uncertainty. This is possible because of progress in recent years in applying Bayesian Hierarchical Modeling (BHM) techniques to geophysical applications where the character of BHM is particularly well suited to addressing measurement and model uncertainty, while quantitatively incorporating significant scientific understanding. A review and examples relevant to geophysics are given in Berliner (2003). Applications discussed there include climate-change and space-time modeling of near-surface ocean winds; also see Berliner et al. 2003.

For our purposes of improving the ABL ADA, BHM provides opportunities for hybrid deterministic/probabilistic modeling and forecasting of complex phenomena that

would otherwise be extremely difficult or impossible. In essence, with BHM, complicated joint probability distributions are modeled as products of simpler, component models. The strategy separates the role of measurement uncertainty from process variability, and it offers direct opportunities for building physics directly into the component models. As such, BHM is a natural framework for organizing the various data sources needed for an improved ABL ADA, including, e.g., rawinsonde, thermosonde, and aircraft measurements, radar, satellite, and possibly other data, compiled or parameterized results from high-resolution DNS and LES of turbulence, as well as theoretical descriptions. The technique is equally valid for 1) post-processing mesoscale-model output to predict C_n^2 along operational paths and 2) as a basis for a probabilistic SGS scheme inside a running mesoscale model.

3.3.1. Bayesian Hierarchical Modeling

The probabilistic modeling approach we employ is based on Bayes Theorem (Bernardo and Smith 1994). To describe the method, we begin with the basic formula

$$[A | F] \propto \int [F | A, Y][A | Y][Y] dY, \quad (2)$$

where $[Y]$ refers to the probability of the occurrence of event Y , $[A|Y]$ is the conditional probability of A given Y , and $[F|A, Y]$ is the joint conditional probability of F given A and Y .

The variable F represents the relevant subset of the resolved mesoscale-model variables, such as the forecast temperature, pressure, wind speed, etc.; i.e., F is our forecast before improvement by BHM. The variable A represents the set of SGS variables being predicted by the model. In other words, A represents an improvement to the forecast F via BHM. Finally, the variable Y represents the set of parameters that characterize the underlying (and unresolved) processes that give rise to A ; e.g., if the process being modeled results from observed atmospheric turbulent mixing layers, then Y can be described by the layer depth L , velocity jump ΔU , altitude Z , etc. Alternately, if the process involves the overturning and breaking of atmospheric gravity waves, then Y would be characterized by the wave amplitude, frequency, and wavelength, as well as the background stratification.

The conditional probability distribution $[A|Y]$ appearing in (1) is called the physics *prior distribution* of A given the unknown variables Y . The conditional joint probability $[F|A, Y]$ in (1) is the so-called *likelihood distribution*. Finally, the output of the model $[A|F]$ is called the *posterior distribution*, which is our probabilistic prediction for A .

Applications of (2) relevant to this project are discussed in §4.3.

4. RESULTS AND DISCUSSION

In this section, we summarize results for our DNS/LES solutions, atmospheric data analysis, and the new BHM approach to probabilistic prediction.

4.1. DNS/LES Solutions

The numerical solutions analyzed for this project were computed over the past ten years, beginning in 1997. Early validation efforts of our wind-shear simulations were conducted with smaller numerical domains than those computed most recently. Nevertheless, comparisons with published and more recently collected atmospheric data have demonstrated that even the early numerical solutions provide a quantitatively accurate description of stably stratified atmospheric dynamics. In §4.1.1., we discuss results from these early validation exercises, and we explain why the DNS solutions at lower Reynolds numbers than those attained in the upper troposphere and lower stratosphere are relevant and useful for ADA development. After addressing solution validation, we next describe the behavior of the computed wind-shear solutions in more detail in §4.1.2. In §4.1.3. and §4.1.4., we discuss the implications of these results for C_n^2 and SGS turbulence modeling.

After describing our wind-shear solutions, we then describe our gravity-wave breaking simulations in §4.1.5. (linear stability problem) and §4.1.6. (nonlinear dynamics). In §4.1.7., we discuss the implications for the wave-breaking solutions on C_n^2 and wave-saturation modeling.

4.1.1. Numerical-Solution Validation

Early wind-shear solutions were computed in domains of size $(\lambda, \lambda/3, 2\lambda)$ in the (streamwise, spanwise, vertical) directions, where λ is the wavelength of the most unstable asymptotic linear eigen mode for the Kelvin-Helmholtz instability. Second-order structure functions were computed for the temperature T and all velocity components (U, V, W) , and comparisons were made with available atmospheric data. Here (U, V, W) are the velocity components in the (x, y, z) directions, where x (y) is aligned in the streamwise (spanwise) direction, and z points in the vertical. The second-order structure function $\Delta_r \psi^2$ for the variable ψ is defined by $\Delta_r \psi^2 = \langle (\psi(\mathbf{x}+\mathbf{r}) - \psi(\mathbf{x}))^2 \rangle$. Here, \mathbf{r} is the spatial separation of two points in the 3D field, and $\langle \rangle$ indicates averaging over the spatial domain of \mathbf{x} . Note, that for very small spatial separations (i.e., $\mathbf{r} \rightarrow \mathbf{0}$), $\Delta_r \psi^2 = \langle (\nabla \psi \cdot \hat{\mathbf{r}})^2 \rangle r^2$, where $\hat{\mathbf{r}}$ is a unit vector in the \mathbf{r} direction. For larger spatial separations, the dependence of $\Delta_r \psi^2$ on r is determined by the spatial statistics of ψ . For example, if the fluctuations in ψ are generated by homogeneous-isotropic turbulence, then $\Delta_r \psi^2 \sim r^{2/3}$ in the inertial subrange for both T and (U, V, W) (Monin and Yaglom 1975). In contrast, for strongly stratified turbulence, Bolgiano (1959) predicts $\Delta_r T^2 \sim r^{2/5}$ and $\Delta_r U^2 \sim r^{6/5}$.

We evaluated $\Delta_r \psi^2$ from the simulation results and fit to the form $\Delta_r \psi^2 = C_\psi^2 r^\alpha$ for separations r in the $r=x$ and $r=y$ directions for $\psi = T, U, V$, and W . Here, C_ψ^2 is the second-order structure constant for ψ , and α is a power-law exponent. We compared our fit parameters with the atmospheric measurements by Kaimal et al. (1972), Gurvich and Zubkovskii (1966), Paquin and Pond (1971), Wyngaard and Cote' (1971), Wyngaard and Pao (1971), and Gibson (1962, 1963). Since none of these atmospheric measurements

evaluated α directly, but rather assumed $\alpha=2/3$, they must be considered as calibrations for the coefficient C_ψ^2 . Nevertheless, this is a useful comparison, as it allows a measure of how well the simulation results capture the magnitude of the inertial sub-range of atmospheric turbulence.

In Werne and Fritts (2000), we reported that: $C_T^2=3.3\varepsilon^{-1/3}\chi$ for both $r=x$ and $r=y$; $C_U^2=2.1\varepsilon^{2/3}$ for $r=x$ and $C_U^2=(4/3)2.1\varepsilon^{2/3}$ for $r=y$; $C_V^2=1.6\varepsilon^{2/3}$ for $r=y$ and $C_V^2=(4/3)1.6\varepsilon^{2/3}$ for $r=x$; and $C_W^2=(4/3)0.9\varepsilon^{2/3}$ for both $r=x$ and $r=y$, during times when the dynamics are nearly statistically stationary. These results are consistent with the atmospheric results for C_T^2 , which are $C_T^2=C_0\varepsilon^{-1/3}\chi$, with $C_0=3.3\pm0.3$ (Kaimal et al. 1972), $C_0\approx3.5$ (Gurvich and Zubkovskii 1966), and $C_0\approx3.3$ (Paquin and Pond 1971). Similarly, atmospheric measurements of $C_U^2=C\varepsilon^{2/3}$ also agree with our results, reporting $C=2.0\pm0.1$ (Kaimal et al. 1972), $C=2.1\pm0.2$ (Wyngaard and Cote' 1971), $C=2.1\pm0.1$ (Wyngaard and Pao 1971), and $C\approx2.1$ (Gibson 1962, 1963). Finally, though some evidence for $C=1.6$ (for V) and $C=0.9$ (for W) was previously reported in the literature (Monin and Yaglom 1975), these results remained somewhat inconclusive until recent aircraft data (Wroblewski et al. 2003) also obtained these same results. It is important to note that this observational verification of the simulation results for C_V^2 and C_W^2 represents much more than a simple calibration of the numerical results. Indeed, the fact that C for U, V, and W are not all equal (not even close) clearly demonstrates that atmospheric turbulence under stably stratified conditions is far from homogeneous and isotropic.

Another valuable aspect of the aircraft measurements reported by Wroblewski et al. (2003) is that they directly evaluated α , and, like the earlier simulation results reported by Werne and Fritts (2000), exponents ranging between $\alpha=2/3$ and $\alpha=2/5$ for T and U were also observed. It should be noted that $\alpha=6/5$ was never seen in either the simulations or the aircraft data; hence, Bolgiano's 1959 theory clearly does not apply.

From the computed 2nd-order structure constants and scaling exponents α , we see that the DNS solutions adequately describe 2nd-order statistics in the inertial sub-range of the atmospheric turbulence spectrum under stable conditions. In addition, because the DNS does not model small-scale quantities and instead must resolve all relevant physical scales of motion (right down to the dissipation scale), we are also able to evaluate the spatial inner scale ℓ_o at which the observed $\alpha=2/3$ or $\alpha=2/5$ laws transition to the $\alpha=2$ law for small separation separations. We did this for all fields analyzed, and we found the following for T and U: $\ell_o(T, r=x \text{ or } r=y) \approx 7.4 \ell_K$; $\ell_o(U, r=x) \approx \sqrt{2} 8.0 \ell_K$ and $\ell_o(U, r=y) \approx 8.0 \ell_K$. Here $\ell_K=(\nu^3/\varepsilon)^{1/4}$ is the Kolmogorov length scale. We note that the temperature inner scale $\ell_o(T)$ was measured previously in the atmosphere, and it agrees perfectly with the DNS result (Hill and Clifford 1978). Also, the ratio of the inner scales deduced from the longitudinal $\ell_o(U, r=x)$ and transverse $\ell_o(U, r=y)$ 2nd-order structure functions, i.e., $\ell_o(U, r=x)/\ell_o(U, r=y) \approx \sqrt{2}$, agrees with nearly isotropic motions at small scales because

$\langle \partial_y U \partial_y U \rangle \approx 2 \langle \partial_x U \partial_x U \rangle$, and hence the smallest spatial scale in x for U is larger than the smallest spatial scale in y by $\sqrt{2}$.

A legitimate and potentially perplexing question regarding these results is “How can DNS at $Re=3 \times 10^4$ simultaneously duplicate 2nd-order structure constants and the inner scales of motion (i.e., quantities that span the broad range of length scales from the tiny dissipation scale up to the largest scales of turbulent motion in the inertial sub-range) when Re can be as large as $Re=10^7$ - 10^8 in the atmosphere?” The answer is that the simulations have achieved sufficient resolution to clearly separate the smallest and largest length scales in the flow. Once such scale separation is achieved, we then expect the scaling behavior for asymptotically large Re to become apparent. Hence, flows with Re spanning a large range of values, but which are all in the same asymptotic scaling regime, can be meaningfully compared once the power-law exponents (e.g., α) and the amplitude coefficients (e.g., C_ψ^2) are known.

4.1.2. Wind-Shear Simulations

The wind-shear simulations were conducted using a constant background temperature gradient $\bar{T}=\beta z$ and a hyperbolic tangent initial streamwise velocity profile $U=U_0 \tanh(z/h)$. The flow was initiated with the most unstable asymptotic linear eigen mode with an amplitude equal to 7% of the maximum initial mean vorticity plus a Kolmogorov noise field with a vorticity amplitude of 1.4%. Cases have been run with a range of Re and Ri values and in domains of varying sizes. Most recently, we have completed runs in domains of size $(4\lambda, 2\lambda, 2\lambda)$, where λ is the most unstable wavelength, for the following Ri and Re values: $(Ri, Re)=(0.05, 2500)$, $(0.15, 2900)$, and $(0.20, 4000)$. Here, Re was chosen so that all solutions required nearly the same number of spectral modes, which peaked at $(n_x, n_y, n_z) = (3600, 1800, 1800)$. These large-domain solutions were computed in order to accumulate statistics for the BHM effort described in §X. We have also completed an exploratory case with $(Ri, Re)=(0.10, 2500)$ in a domain of $(\lambda, \lambda, 2\lambda)$ so that we may determine the value of Re to use in the larger domain (it is $Re=2800$), and so that we may get a glimpse of the solution behavior for $Ri=0.10$.

Flow Morphology and the Transition to Turbulence

The overall evolution for the four cases discussed above is summarized in Figures 3-10. Figures 3-6 show the temperature on both a streamwise-vertical cut and on the mid-plane at seven distinct times during the flow evolution. Figures 7-10 show the vorticity magnitude at the same times and locations. From both fields (temperature and vorticity), we see the clear influence of stratification as Ri is varied. Most obvious is the reduced layer depth for higher Ri . This is because the stronger stratification at higher Ri impedes vertical motion, suppressing layer vertical growth. In addition to this continuous trend with Ri , we also see that a fundamental change occurs between $Ri=0.10$ and $Ri=0.15$. For the lower values of Ri , we see laminar billow cores persist later in the flow evolution, while turbulence erodes the braid regions between billows first. Only later do the cores become fully turbulent. In contrast, for the higher values of Ri , the braids persist intact longer, while turbulence develops in the cores first. This difference has potentially

important consequences for both mechanical and optical turbulence generation and evolution.

To understand how this shift in turbulence initiation between the billow and braid regions can have important consequences, consider that persistent billow cores act as strong organizing agents for the flow. At low Ri , the billows are large and roughly circular in cross section and, as a result, they rotate more like solid bodies than their higher Ri counterparts. The low- Ri billows therefore are stabilized longer by a flywheel effect, and, thus, are able to extract more kinetic energy longer from the background shear flow, leading to more intense turbulence and vigorous mixing, which impacts the structure and evolution of the layer's C_n^2 profile.

The stabilization of the billow cores by rotation also leads to a contorted and somewhat counter-intuitive transition to turbulence that gives rise to two distinct episodes of intense turbulence eruption, while the higher Ri cases display a simpler transition characterized by only a single episode of intense turbulence growth and decay. To explain these distinct pathways to turbulence, we begin with the simpler case of high Ri . In this case, as soon as billows form and undergo their first rotation, the initial background stable stratification in their cores becomes convectively unstable as the billows rotate through 180° . Since the strong stratification at high Ri suppresses vertical motion and overturning, these high- Ri billows are compressed in the vertical direction and, hence, they are not stabilized by solid-body rotation like their lower- Ri counterparts. As a result, high- Ri billows develop turbulence in their cores nearly immediately upon formation. Meanwhile, their braid regions remain intact. This is intuitive, as the enhanced vertical compression of the braid region (resulting from adjacent billow formation) makes the braids the most (convectively) stable part of the flow. When the turbulence from the billow cores is sheared out of the cores and migrates into the braids, then the braids themselves become unstable.

In contrast, the transition to turbulence for the low- Ri billows is more complex. Though the billow cores are the most convectively unstable regions in the flow, they remain stable due to their solid body rotation. This allows the billows to wind up fluid of alternating density and vorticity at their periphery so that strongly layered density and spanwise vorticity develops while the billows remain laminar. Eventually the local Rayleigh number in the billow edges becomes sufficiently high for convective instability to develop in the edge regions of the billows. This instability takes the form of streamwise-aligned counter-rotating convection rolls that wrap around the billows. The billow edges therefore become turbulent first, triggering instability in the adjacent braid regions, despite the enhanced stable stratification in the braids. Billow-core stability persists because of the stabilizing influence of rotation, but eventually the billow cores also become unstable, and when they do, turbulent kinetic energy spikes.

These contrasting transitions to turbulence are evident in Figure 11, which shows the time evolution of the volume-integrated kinetic (KE, solid curve) and an estimate of the potential energy (PE, dashed curve) per unit volume, along with the maximum values of

the three vorticity components ω_i for all four cases discussed above. The vertical dotted lines correspond to the times shown in Figures 3-10.

In Figure 11, the background mean velocity and temperature have been removed, hence,

$$KE = (L_x L_y h)^{-1} \int \left[(U - \bar{U})^2 + V^2 + W^2 \right] d^3x \quad (1)$$

$$PE = (L_x L_y h)^{-1} Ri \int (T - \bar{T})^2 d^3x \quad (2)$$

The normalization factor $L_x L_y h$ includes the horizontal extent of the layer $L_x L_y$ in order to correct for the effect domain size has on the integrated energy. We use h for the vertical length instead of L_z because the turbulent motions do not fill the full depth of the simulated domain. The vorticity maxima indicate when turbulent fluctuations and mixing are active.

Panel (a) in Figure 11 (for $Ri=0.05$) exhibits the two-peak episodic nature of KE and PE for weak stratification described above. The strong second peak occurs when turbulence finally erupts in the billow cores for this case. This is very different from the $Ri=0.10$ case, for which we see that billow and braid turbulence occur nearly simultaneously (see Figures 4 and 7), and hence only one large peak is evident in both KE and PE. For $Ri=0.15$ and 0.20 , billow turbulence clearly develops first, and the braids become unstable relatively later (see Figures 5, 6, 8, and 9). In these cases, there is mild evidence for the distinct timing of braid and billow turbulence in PE, but the effect is not nearly as pronounced as it is for $Ri=0.05$. The reason for the difference is that the weakly stratified structure of the billow cores is conducive to the production of copious amounts of turbulent KE, while strongly stratified braids are not.

Other noteworthy features in Figure 11 are : 1) the coincidence of the highest small-scale turbulence intensity (as is evident in the largest vorticity fluctuations) with a local suppression of PE due to vigorous turbulent mixing; 2) more rapid initial KE and PE growth for lower Ri ; 3) much higher KE and PE maxima for low Ri ; and, curiously, 4) a non-monotonic dependence of the peak vorticity on Ri (i.e., vorticity fluctuations peak at values of approximately 70, 45, 60, and 47 for Ri of 0.05, 0.10, 0.15, and 0.20, respectively – see Figure 11).

Flow Profiles for High and Low Ri

Additional evidence of important differences in the flow at high and low stratification can be seen in the evolution of profiles for first- and second-order properties. These are shown in Figures 12 and 13 for $Ri=0.05$ and $Ri=0.20$, respectively. The left panels of the figures show the time evolution of the mean temperature deviation $T-z$ and the streamwise velocity as functions of height. z is the initial profile for T , therefore $T-z$ is the deviation of T from its initial profile. The curves for $Ri=0.05$ (Figure 12) and $Ri=0.20$ (Figure 13) are separated by 20 and 10 time units, respectively. The buoyancy time scale for these two cases differs by a factor of two, explaining the difference in the time units we chose. The middle panels in the figures show the normalized temperature and velocity variance, i.e., the variance divided by its maximum. The right panel shows the maximum used to normalize the variance curves in the middle panels. In the figures,

$\langle qq \rangle = \langle (U - \bar{U}(z))^2 + V^2 + W^2 \rangle$ is the sum over the three velocity components. Also, $\max\langle TT \rangle$ has been multiplied by Ri in the right panel so that each of the two curves represents a contribution to the total energy, which is approximated by $E = (q^2 + Ri T^2)/2$. As is evident from the decay with time shown in the right panel, normalizing the variance curves is necessary to see the variation with height of the profiles at late times.

The figures show that the mean velocity and temperature are modified significantly during the course of the flow evolution. The deviation in the mean temperature exhibits a characteristic S-shape, with the $Ri=0.05$ ($Ri=0.20$) layer growing from 2h to roughly 6h (3h) in depth; i.e., the higher Ri layer experiences significantly less growth. The mean velocity in both cases approaches a nearly constant gradient, though deviations from a strictly linear profile at late times are easily discernible, especially for $Ri=0.05$. This occurs because of the vigorous mixing at midlayer (see the lower middle panel of Figure 12), which produces positive curvature in $U(z)$ at $z=0$. The variance in temperature (upper middle panels) exhibits peaks near the top and bottom of the turbulent layer. This occurs because the mean temperature gradient is expelled from the middle of the layer by turbulent mixing, and it accumulates at the edges as a result. Where the mean temperature gradient is large, so too is the potential for producing temperature variance. Note the inverse relationship between the temperature and velocity variances for $Ri=0.05$: whereas the velocity variance peaks near midlayer and is understandably weaker near the layer edges, the temperature variance has the opposite behavior, i.e., it attains its maximum near the layer edges, and is minimal near the middle of the layer. This inverse relationship is notably absent in the higher Ri case (Figure 13). Instead, for this case $\langle qq \rangle$ and $\langle TT \rangle$ appear to have nearly identical shapes. Also significant is the much smaller magnitude for $\langle TT \rangle$ in the higher Ri case; compare the right panels of Figures 12 and 13. The reasons for these stark differences are 1) the relative efficiency of mixing for the two cases (mixing is initially much more efficient for lower Ri) and 2) the relative depths of the two layers (lower Ri results in deeper layers). This second effect insures that the higher Ri case will retain strong velocity gradients, especially in the edge regions of the flow (see lower left panel of Figure 13 at the middle time shown, which is $t=80$). As a result, the local stability profile (i.e., the diagnosed Richardson number versus height) for this case dips back below the stability limit of $Ri(z)=0.25$ near the edges, reinvigorating the dynamics in the edge regions and giving rise to renewed turbulence KE production there. This is remarkable because at a slightly earlier time ($t=70$) the entire stability profile had already been elevated above $Ri=0.25$, indicating that the time of active dynamics had already passed.

The right panels of Figures 12 and 13 clearly demonstrate that the lower Ri case ($Ri=0.05$) experiences extremely rapid instability growth and higher energies compared to the high- Ri case.⁵ We also note that stratification has a much more evident impact on the developing dynamics for the higher Ri case because PE is larger than KE during the initial growth phase for $Ri=0.2$; this is not the case for $Ri=0.05$. Finally, the decay in

⁵ In these panels, the time scale is a factor of two larger for the lower Ri because the buoyancy time is proportional to \sqrt{Ri} .

energy is exponential and rapid for $Ri=0.2$, while it is much more gradual for $Ri=0.05$, and it appears to experience a shift in the controlling dynamics at $t=250$ (see the change in the decay behavior in the upper right panel of Figure 12).

Universal Aspects of Turbulent-Shear-Layer Evolution

Given the dramatic differences in turbulent-shear-layer evolution for strong and weak stratification discussed above, the prospect of developing a reliable description that can be used as the bases for a traditional SGS approach is daunting. When resolution is coarse (as is always the case for mesoscale NWP models), the SGS modeling challenge is compounded because, in this case, even the gross behavior of the shear layer's large-scale dynamics and evolution must be modeled; i.e., the modeling task is not simply confined to the smallest scales of motion in the inertial range of turbulence.

Thankfully, despite the significant differences that accompany different Ri , we have discovered through our DNS work that certain characteristics of shear-layer evolution are universal or nearly universal. To demonstrate this, in this section, we describe the end-state profiles of our $Ri=0.05$ and $Ri=0.20$ simulations and discuss how aspects of these profiles can be correctly anticipated. To begin, Figure 14 shows the $Ri(z)$ profiles for the highest and lowest Ri simulations ($Ri=0.20$ and $Ri=0.05$). The dotted (solid) line depicts the initial (final) Ri profile. The time selected for the final profile is after the turbulent dynamics have subsided and the flow has achieved a restratified end state. The final time for $Ri=0.05$ is a factor of two larger than that for $Ri=0.20$, compensating for the differing buoyancy periods for the two cases; i.e., when time is scaled by the buoyancy frequency N , the end time Nt is identical for the two cases. From the figure, we note that the initial layer is only 1.29 times deeper for the $Ri=0.05$ case, however, by the final time, the ratio of the layer depths is significant; i.e., the $Ri=0.05$ layer becomes 2.23 times deeper than the $Ri=0.20$ layer at the final time. The fact that the lower Ri case results in a deeper shear layer is not surprising, given that the stronger background stratification for the $Ri=0.20$ case inhibits deeper growth.

In order to explore the evolution of $Ri(z)$ with time (not just the initial and final states), Figure 15a shows the midlayer ($z=0$) Ri values for these two cases. Here, we see that both layers seemingly approach similar values at late times. It is interesting that this value is approximately $Ri=0.55$, i.e., well above the neutral stability limit of 0.25. It is also somewhat alarming that at intermediate times the evolutions are clearly quite different, and in particular, that the $Ri=0.20$ case significantly overshoots neutral stability and actually rebounds to a less stable end state than it attains at intermediate times.

In an attempt to explain this strange behavior, we consulted the flow visualizations (e.g., Figures 3-6) and determined that the $Ri(z)$ profile is inadequate for completely describing the layer stratification. The difficulty lies in Ri 's definition, which includes only vertical gradients of temperature and velocity, while the persistent braids for the $Ri=0.20$ case provide significant horizontal strain-rate gradients that can feed turbulence production for a significant amount of time. Therefore, we considered a generalization of Ri by defining the nondimensional time-scale ratio N/S , where N is the buoyancy

frequency, and $S=(S_{ij}S_{ij})^{1/2}$ is the magnitude of the large-scale strain rate $S_{ij}=\langle\partial_i U_j + \partial_j U_i\rangle_y$. Here, $\langle \rangle_y$ refers to averaging in the spanwise direction only. We note that because of the factor of $1/2$ in the definition of S_{ij} , at the initial and final times when the mean flow is horizontally homogeneous and gradients in z are the only gradients present, S will be only half the size of $\partial_z \bar{U}$, and therefore $(N/S)^2$ will be roughly twice as large as Ri , or $N/S=\sqrt{2} Ri$.

Figure 15b depicts the mid-layer value of N/S versus Nt . From the plot, we immediately notice that the overshooting evident in Figure 15a has been removed, indicating that our suspicion that neglecting the influence of horizontal strain-rate gradients was indeed to blame for the odd behavior of $Ri(z=0)$. We also see that the final restratified value for N/S appears to be very near 1.0. This is extremely encouraging, as it indicates that the dynamical evolution of the layer halts when the time scale associated with the evolving large-scale strain rate (i.e., S^{-1}) drops sufficiently for it to be overtaken by the buoyancy time scale (i.e., N^{-1}). Once this happens, buoyancy's role in resisting vertical motion is satisfied and a balance between the potential destabilizing influence of large-scale kinetic energy and the stabilizing influence of stratification is achieved.

Extending this analysis further, we developed a very simple model of a layer's final depth based solely on energetics arguments. If one assumes horizontally homogeneous initial and final states, it is trivial to show that the final layer depth L should scale with N/S . This is explicitly demonstrated with Figure 16, which shows L versus Ri for the DNS solutions. The data points show the results for the four Ri cases considered, while the curve is a fit to the form $L=C_1 Ri^{-1/2} + C_2$ with $C_1=1.5$ and $C_2=-0.5$.

The two results $N/S \approx 1$ and $L \sim Ri^{-1/2}$ will be useful in developing the BHM model described in §3.3.1.

4.1.3. Gravity Wave-Breaking Simulations

In addition to the wind-shear simulations discussed above, we also conducted series of wave-breaking simulations as a part of this project. The results from the wave-breaking work focused on instability structures and the transition to turbulence resulting from overturning gravity waves and the role such breaking waves play in producing turbulence layering in the atmosphere (Fritts et al. 2003, 2006, 2007).

Figure 17 shows a sequence of images of vortex tubes that develop in a recently computed wave-breaking event. The left column of images show the side view of the wave with the numerical domain tilted to coincide with the phase of the wave, while the right panels show the end-view of the edge of the domain. Though the wave propagates relative to the numerical domain, the images have all been shifted so that the wave phase is shown fixed, with the primary wave sinusoidal velocity upward and to the left in the upper half domain of the left column and downward and to the right in the lower half (again, describing the orientation in the left column). The amplitude of the wave A is such that a portion of its phase is statically unstable by 10%; i.e., $A=1.1$. For this solution, instability sets in first just above the region of lowest static stability as the wave

propagates. The dominant instability structures take the form of horizontally-aligned, streamwise-oriented vortex tubes, similar to the predicted most-unstable eigen mode computed for this particular wave (Lombard and Riley 1996). Also, significant interactions with secondary waves are also observed. The initial vortex tubes interact and trigger a cascade to smaller scale motions, rapidly erupting into very intense turbulence at small scales. The turbulence moves through the flow as the wave propagates.

Many similarities exist between the wind-shear results discussed above and the wave-breaking solutions described here; these include: 1) the presence of streamwise aligned vortex tubes which derive KE from buoyancy and shear sources, 2) transitions to turbulence via vortex interactions common to both flows, 3) expansion, mixing, and influences of turbulence far beyond the initial regions of instability, 4) turbulence duration of several buoyancy periods or less, 5) sharp gradients in turbulence quantities in edge regions, and 6) spatial separation of the peak turbulent kinetic energy and thermal dissipation (indicating separation of strongly mixed regions from C_n^2 concentrations). This last effect implies that optical turbulence impacts will not be coincident with the most intense regions of mechanical turbulence, but instead will adjoin such regions. Important differences between the wind-shear and wave-breaking results are also present, the most immediate being that wind-shear events are localized in altitude, while waves propagate. As a result, wind-shear turbulence permits the development of sharper edge regions and larger peaked concentrations of C_n^2 ; while low-frequency gravity waves may also have this characteristic, higher frequency waves propagating at shallower angles move continuously through altitude, sweeping turbulence through the fluid following the phase of the breaking wave.

The most important result from this work is the very similar evolution of a companion simulation conducted with $A=0.9$ (see Figure 18). Though clear differences between the two solutions exist (Fritts et al. 2007), conventional wave-saturation theory (Dunkerton 1989) predicts that this second simulation should not exhibit instability at all. This is because wave-saturation modeling takes the view that waves that are everywhere statically stable are also dynamically stable. The work of Lombard and Riley (1996) has relatively recently shown that this idea is errant; however, they also demonstrate that the linear growth rates for low amplitude waves is lower than high amplitude waves, so it has been unclear until now (with our simulations) just how misleading current linear saturating modeling is. Most importantly, while saturation modeling would predict that the $A=0.9$ wave would remain stable while the $A=1.1$ wave would experience an amplitude reduction to $A=1.0$, and then become stable, our simulations show that actually both solution experience significant amplitude reductions to $A=0.3$ before saturating. This is very far from conventional saturation models, and indicates how important simulations like these will be in developing more reliable and accurate models in the future. For more details on the wave-breaking solutions, see Fritts et al. (2007).

4.1.4. Implications of DNS Simulations for C_n^2 and SGS Modeling

Figure 19 shows a sequence of thermal and viscous dissipation images for wind-shear simulations with $Ri=0.05$. This image clearly communicates the nature of mixing in

stratified flows. Whereas mixing is vigorous where the viscous dissipation is large (orange regions), the thermal dissipation is weak in these regions. This is because strong gradients in velocity have homogenized the thermal field at the core of the billow, and thermal gradients therefore are relegated to the edges of the layer. Since thermal and index-of-refraction gradients are intimately related, this result reveals that optical turbulence will also be concentrated in the regions shown in blue in the figure.

This is problematic for optical turbulence forecasting because the edge regions of a stratified shear layer are particularly challenging to model. First, these regions are situated in the transition zone between quiescent laminar flow exterior to the shear layer and turbulent flow inside the layer. As a result, the typical mathematical assumptions made in turbulence modeling (namely homogeneity, isotropy, and stationarity) are all known to be false in this region. Furthermore, stratification remains challenging to model, even at small scales, and the edges of the layer harbor the highest mean stratification levels at intermediate and late times. This means a sophisticated approach to modeling is required in this region. We note that the new results shown in Figure 13 at high stratification levels (i.e., $Ri=0.20$) indicate that strong velocity fluctuations also reside in the edge regions at intermediate times. This potentially amplifies the challenge because it implies that accurate solutions require realistic descriptions of both the temperature and velocity fields, and one cannot make a weak-flow assumption for the velocity, which might have been possible at lower Ri (see Figure 12).

4.1.5. LES Solutions and Turbulence Modeling.

As part of this project, we also conducted LES of the same problems for which we computed DNS solutions. Our initial plan was to refine the LES SGS model sufficiently for stratified flow to use the LES code in place of the much more expensive DNS code to compute solutions and accumulate the statistics needed for the BHM parameterization approach. After some refinement of the LES code and detailed comparisons with the DNS solutions, we made progress on describing the dynamics during the periods when the turbulence is most intense, but had difficulty getting the solutions to match when the LES was started from $t=0$ with the same initial conditions as the DNS.

Figure 20 demonstrates this by presenting results for three sets of comparisons. The top row of panels in the figure shows results for a TKE SGS model for the LES. The left panel shows the resolved-scale kinetic energy (KE) for the DNS (red) and LES (blue) solutions. The right panel shows the eddy viscosity (red) and eddy diffusivity (blue) for the LES (solid line) and filtered DNS (data symbols) fields. Though the LES appears to track the DNS resolved-scale KE reasonably well on average (upper left panel), it is clearly much too viscous and diffusive, with eddy transport coefficients that are 8.5 times larger than the DNS values (upper right panel). The dynamic-Smagorinsky-model results (middle row of panels) are far superior at estimating the eddy-transport coefficients, being only 10-15% too large when turbulence is most intense (from $t=120$ to 180), and only a factor of 2 too large (on average) at earlier and later times. Nevertheless, the dynamic-Smagorinsky model clearly under-estimates the resolved-scale KE when 3D

instability develops (from $t=50$ to $t=80$) and at later times during the turbulent decay phase of the flow (middle-left panel).

Some causes for concern for the LES approach include: 1) the initial deviation of the solutions just before $t=50$, when 3D instability of the flow first appears, 2) the subsequent detachment of the phase of KE oscillations for the DNS and LES solutions (middle-left and top-left panels from $t=80$ to $t=150$), 3) the over-estimate of SGS turbulent transport at late times, and 3) large spikes in the LES SGS transport coefficients that do not exist in the DNS solutions. Though some of these effects appear to be systematic and representative of the SGS models used, others may be a direct result of the inadequacy of the modest domain used ($\lambda \times \lambda/3 \times 2\lambda$) to produce sufficiently stable statistics so that meaningful DNS/LES comparisons can be made. For this reason, and to ensure that we will be able to use the DNS to accumulate statistics for the BHM approach, we conducted simulations in much larger domains of size $4\lambda \times 2\lambda \times 2\lambda$, i.e., a full 24 times larger. Results for the DNS and the dynamic-Smagorinsky LES are shown in the bottom row of Figure 20.

From Figure 20, we see that KE oscillations are significantly reduced in the large domain (bottom-left panel), indicating the significantly improved statistics for the increased domain size. The departures of the LES from the DNS that remain can be clearly identified, and speculation regarding the potential role of inadequate spatial statistics is no longer a concern. The differences between LES and DNS that persist include 1) a systematic under-estimate of resolved-scale KE from just after the onset of 3D instability ($t=37$) to the eruption of turbulence in the billow cores ($t=86$), 2) a systematic over-estimate of resolved-scale KE from $t=110$ onward during the turbulence decay phase of the evolution, and 3) sizeable spurious spikes in the LES eddy-transport coefficients during the development of 3D instability.

The overestimate of the eddy coefficients when 3D instability develops is understandable and is actually impossible for the LES to avoid. It results when sharp laminar gradients form that simply must be resolved by increased grid resolution. Unable to resolve these high-Re laminar features, the SGS model interprets them as resulting from turbulent motions, and eddy transport (erroneously) spikes as a result. Furthermore, with eddy transport grossly over estimated, KE dissipation is elevated, and resolved-scale KE is errantly depleted as a result. Therefore, the LES' inability to properly describe the onset and development of the 3D instability structures in the flow produces both the large spike in the eddy-transport coefficients and the dip in resolved-scale KE. It seems clear that no improvement to the LES SGS model will be able to address this difficulty, and DNS will be required to represent this period in the flow's evolution. This is unfortunate, as the resolution requirements during this time are as high as at any later time, even when turbulence is at its most intense.

The overestimate of resolved-scale KE during the turbulent decay phase is interesting because it is not evident for either of the LES SGS models in the smaller domain. This indicates that this aspect of the numerical solutions cannot be reliably evaluated and analyzed in the smaller domain. Continued analysis of the new solutions in the larger

domain is required to understand the over estimate of resolved-scale KE (and PE – not shown) and the simultaneous over estimate of the eddy-transport coefficients at late time. Differences between these solutions for $Ri=0.05$ and the other Ri values must also be evaluated.

Despite these deficiencies with the LES solutions, there are reasons for encouragement. Most importantly, the differences in second-order quantities (like resolved-scale KE) between the DNS and LES solutions are modest. Hence, we expect second-order structure functions to be reasonably well described by the LES. Indeed, Figure 21 presents comparisons of fit parameters for the second-order structure functions for the DNS and LES, and the results appear to agree sufficiently for the LES results to be directly useful. This is an exciting result, as the LES employed 6 times fewer grid points in each spatial direction compared to the DNS, translating into a factor of 1300 less computer time required to obtain the result. Nevertheless, optimism should be tempered until an observed dependence on the filter width is understood and can be anticipated ahead of time. Until then, calibration of the LES (via judicious choice of the number of grid points used) will be required.

4.2. Atmospheric Data Analysis

The BHM approach described in §3.3. and §4.3. requires statistical information that meaningfully quantifies 1) the likelihood of turbulence-generating processes in the atmosphere and 2) the nature of the turbulence resulting from these processes. The results of the data analysis presented in this section directly address the first point, by measuring probability density functions (PDFs) that characterize atmospheric turbulence layers, and indirectly addresses the second, by providing comparisons with the DNS/LES solutions so that we may be confident the simulated dynamical processes are directly relevant to atmospheric dynamics.

Two data sources were used in the data analysis associated with this project. These include 1) rawinsonde balloon data and 2) aircraft measurements of atmospheric turbulence. The data and analysis methods are described in §3.2. Here, we present the results of those analyses.

4.2.1. Balloon-Data Analysis

Figure 22 shows probability density functions resulting from the analysis procedure described in §3.2.1. The upper left panel shows the PDF for the layer depth L , which was obtained by locating the local maxima and minima of the strain rates $\partial_z U$ and $\partial_z V$ associated with the measured wind field (see §3.2.1.). The upper middle and lower left panels show similar results for the velocity jump ΔU and the layer's altitude Z . The remaining three panels show additional information, including the temperature drop ΔT (upper right panel), the layer's bulk Richardson number Ri_L (lower right panel), and the layer Reynolds number Re_L (lower middle panel). Each plot shows three curves, where the solid curve represents results obtained when using all of the data, while the dashed and dotted curves are for the stratosphere and troposphere only.

These initial results are extremely encouraging for using probabilistic methods to evaluate atmospheric quantities. In particular, all of the PDFs are well-defined, and in addition those for L , ΔU , and ΔT have nearly perfect universal shapes. To see this, in Figure 23, we have re-plotted the results using the reduced variable $X'=(X-\langle X \rangle)/X_{\text{RMS}}$, where X represents any of the variables plotted, and $\langle X \rangle$ and X_{RMS} are its mean and root-mean-squared values, respectively. When the PDF is invariant in its reduced variable X' , it can be parameterized solely by its mean and RMS values $\langle X \rangle$ and X_{RMS} , significantly simplifying the modeling effort. Nevertheless, the mean and RMS values differ notably between the troposphere and stratosphere, and they exhibit some small variation with location and probably season as well. For example, stratospheric layers are less likely to be deep, but they have higher velocity and temperature drops across them. Their Reynolds numbers are less than for the troposphere, consistent with the troposphere's weaker stratification (and therefore its more vigorous turbulence). More work is required to determine and parameterize the seasonal and locational dependencies. However, the remarkable similarities we observe when data from individual sites (from Utah to Kansas!) are compared, indicates that the dynamics aloft are fairly robust and should be successfully modeled by this kind of approach.

4.2.2. Aircraft-Data Analysis

Figure 24 shows a plot of cliff-ramp structures in the measured potential temperature reported by Wroblewski et al. (2003) for a flight over Wales through the bottom of the jet stream at an altitude of 11.4km. The measured atmospheric data are shown in the left column of panels for (from top-to-bottom) potential temperature θ , streamwise velocity U , spanwise velocity V , and vertical velocity W . Distinctive structures like these have been observed in 11 data sets collected over Australia and England, and more continue to be discovered as analysis of the data progresses.

The form of the structures shows a clear sawtooth shape in θ that coincides with a subsequent increase in U and suppression of fluctuations in W . The sawtooth pattern in θ is immediately identifiable from Figures 5 and 6 as the temperature jump in the braid region between billows. As the braids remain intact longer for the higher Ri cases, it is more natural to identify this sawtooth feature with the $Ri=0.15$ and $Ri=0.20$ cases we have computed. The right column of panels in Figure 24 shows that this is indeed the case for a path through the DNS data at $t=77.8 h/U_0$ for $Ri=0.20$. Similar features are evident for the $Ri=0.15$ case at $t \approx 72 h/U_0$, but such events become more rare in the DNS as Ri is decreased further, and they are completely absent by $Ri=0.05$. Similarly, the suppression of W fluctuations near the braid region is a characteristic of high- Ri solutions where instability sets in first in the billow cores (see Figures 9 and 10). In contrast, the lower Ri cases possess fluctuations that are substantial near the braids, and at $Ri=0.05$ a large-scale variation in W is observed. This, combined with the absence of cliff-ramp or sawtooth structures, rules out $Ri=0.05$ as a candidate value of Ri for the aircraft data in Figure 24.

We can refine these qualitative observations further in an attempt to assign a specific value of Ri to the observations. We do this by quantitatively comparing more features in the flight data to match, in fingerprint fashion, similar paths through the DNS. We begin by deducing the wavelength λ evident in the observations. By evaluating data from the three BAT probes, it was determined that the aircraft traveled roughly 12° off of the streamwise direction (Wroblewski 2007). With a flight speed of 97.5 m/s, the time-trace data is converted to spatial data, and λ is determined to be $\lambda=1.63$ km. Also, from the temperature measurements during ascent, the potential temperature gradient is measured to be $\beta=7.0$ K/km. Finally, from the first sawtooth at $x=74.6$ km in Figure 24, we obtain the following discernable characteristics: a temperature drop of $\Delta T=2.8$ K, a velocity jump of $\Delta U=5.5$ m/s, and a drop in ΔT by 0.75 at $x=79.6$ km (corresponding to the passage of $\Delta t=51.3$ seconds).

Similarly, from the DNS results in Figure 24 for $Ri=0.20$ (and from similar results for $Ri=0.15$) [and for $Ri=0.10$], we obtain the following: $\lambda=9.5$ h (10.3 h) [11.3 h]; $\Delta T=0.9$ βh (1.65 βh) [0.6 βh]; $\Delta U=0.64$ U_0 (0.7 U_0) [0.3 U_0]; all at $t=77.8$ h/ U_0 (72.2 h/ U_0) [81.2 h/ U_0]; and a reduction in ΔT to 75% of its initial value over a time span of $\Delta t=5.2$ h/ U_0 (3.9 h/ U_0) [3.7 h/ U_0]. While these quoted quantities were straightforward to determine from the virtual flight paths through the DNS for $Ri=0.20$ and $Ri=0.15$, they were more challenging to obtain from the $Ri=0.10$ case (and admittedly required some imagination).

From these data, we can estimate the value of h for the observed shear layer by setting the DNS and aircraft wavelengths equal to each other. In this way we obtain $h=172$ m (158 m) [144 m] from the $Ri=0.20$ (0.15) [0.10] DNS results. Similarly, by equating the DNS and aircraft temperature drops ΔT , we obtain $\beta=18.1$ K/km (10.7 K/km) [32.4 K/km]. From the direct measurement of $\beta=7.0$ K/km, we see that Ri must be between $Ri=0.10$ and $Ri=0.15$. Furthermore, we note that with the dramatic increase in the prediction of β for the $Ri=0.10$ case, we conclude that Ri cannot be as low as $Ri=0.10$ for the aircraft measurements. By simply extrapolating the $Ri=0.15$ and $Ri=0.20$ cases, we obtain $Ri=0.13$ for the aircraft data. Also, if we perform similar analysis attempting to match the decay of ΔT over time, we estimate Ri must be greater than $Ri=0.11$.

More analysis and comparisons between the DNS results and the aircraft measurements are required to refine these estimates further. This is part of our ongoing work, because comparisons like these will permit us to construct the census information needed for the BHM approach described in the next section.

4.2.3. BHM Approach to Probabilistic Prediction

The basic approach of a BHM was described briefly in §3.3.1 with Equation (2), which contained the variables A , F , and Y . In the approach, A represents the quantity we are modeling. For this project, it is a measure of optical turbulence (e.g., $A=C_n^2$) or the SGS quantities needed to improve the AFWA mesoscale model (e.g., $A=\tau_{ij}$ or h_i , where τ_{ij} is the SGS Reynolds stress and h_i is the SGS heat flux). F is the set of mesoscale-model forecast variables (e.g., pressure, temperature, wind fields, etc.) or diagnostic

quantities based on these (e.g., the model-predicted C_n^2 profile, or $(C_n^2)_M$, the model-predicted Ri or Ri_M , etc.). Lastly, Y describes the unresolved processes that contribute to the existence of A . For example, for atmospheric mixing layers, Y could include the layer depth L , its altitude Z , velocity jump and temperature drop ΔU and ΔT , initial layer Richardson number $Ri^{(0)}$, the layer Reynolds number Re_L , the background stratification N^2 , and the layer's age a . For gravity waves, Y would encompass the spectrum of wavelengths and frequencies present, their associated amplitudes, and the wind and stability profiles through which the waves will propagate.

When considering these lists of variables proposed to define Y , immediately we note that some of the quantities are redundant. For example, in the case of atmospheric mixing layers, if we know the location Z of a layer, then its mean viscosity $\nu(Z)$ can be estimated; hence, knowing ΔU , L , and Z , we can compute the layer Reynolds number $Re_L = \Delta U L / \nu(Z)$, demonstrating that Re_L is not a linearly independent variable required in the set Y if Y already contains ΔU , L , and Z . Furthermore, if we know Re_L and $Ri^{(0)}$, then we can use the DNS solutions to determine the non-dimensional layer depth L/h and the non-dimensional temperature drop $\Delta T / (\partial_z \bar{T} h)$ as a function of time. Using these quantities and the fact that $(N/S)^2 \approx Ri_f \approx 1/2$ (where Ri_f is the final layer Richardson number – see §4.1.2 and Figure 15b to understand the value $\approx 1/2$), then we can estimate h (from L/h) and N^2 from the approximation

$$\frac{N^2}{(\Delta U)^2} \left(\frac{\Delta T}{\partial_z \bar{T} h} \right) Lh \approx \frac{1}{2}, \quad (3)$$

which follows directly from $Ri_f \approx 1/2$. Noting these relationships, we can remove all redundancy in the proposed set Y and use only the five variables $Y = (\Delta U, L, Z, Ri^{(0)}, a)$. The detailed implementation of this set for Y is accomplished via repeated application of Bayes Theorem, so that evaluation of $[Y] = [L, \Delta U, Ri^{(0)}, a, Z]$ can be organized by computing the individual component distributions contained in

$$[Y] = [L | \Delta U, Ri^{(0)}, a, Z] [\Delta U | Ri^{(0)}, a, Z] [Ri^{(0)} | a, Z] [a | Z] [Z] \quad (4)$$

The final step in developing a BHM for C_n^2 involves determining which set of forecast variables F in Equation (2) are sufficient to construct the algorithm. Decisions as to which variables are needed will be based on the results of experimentation once the model is implemented and tested. The set F will evolve as we learn more from the results of these tests.

Even though we do not know which variables F will be included in the final implementation of (2), we can still describe the procedure for building the conditional PDFs identified in (2), and we can describe the procedure for solving the model.

First, the *physics prior* distribution $[Y]$ has already been determined in the limit of Equation (4) when all component variables in Y are independent, i.e., Equation (4) reduces to $[Y] = [L][\Delta U][Ri^{(0)}][a][Z]$. The individual component distributions for this case are presented in Figures 22 and 23. More detailed statistical analysis of the rawinsonde data is required to evaluate Equation (4) more completely. Next, the *physics prior* distributions $[C_n^2 | Y]$ must be computed from the DNS. Preliminary evaluations have

already been computed based on second-order structure functions from the DNS (Werne and Fritts 2000). As was stated in §4.1.1., these DNS second-order structure function results have been validated against atmospheric tower data and aircraft data, and they have been shown to be in perfect agreement with the atmospheric measurements. Finally, the remaining *likelihood distribution* $[F | C_n^2, Y]$ on the right-hand side of Equation (2) represents an estimate of the dependence of the relevant forecast variables F on the actual C_n^2 field and the Y associated with unresolved atmospheric mixing layers. This can easily be determined from compiled rawinsonde data by 1) determining the properties Y from the data (which we have done when constructing the PDFs presented in Figures 22 and 23) and then simply filtering the raw data to the mesoscale model's spatial resolution, and computing F from the result. For example, if a method for estimating the model-predicted C_n^2 profile, i.e., $(C_n^2)_M$, is used [e.g., Dewan et al. (1993) or Jackson (2004), models currently used by the Air Force], then $F=(C_n^2)_M$, and computation of $[F | C_n^2, Y]$ is nothing more than a filtering procedure applied to $(C_n^2)_M$.

4.2.4. Intrinsic Limitations of Deterministic NWP Modeling

Mesoscale NWP forecast models rely on SGS descriptions of unresolved processes. These models correctly acknowledge that increased atmospheric stability leads to reduced small-scale vertical transport and mixing. As such, the SGS models used all include a dependence on Ri for the model mixing length, and they effectively turn off SGS turbulent transport when the atmospheric Richardson number is above that needed for instability processes to become active. For the gradient Richardson number, this would result for flows with $Ri > 0.25$. However, the models typically use somewhat larger values of the bulk Richardson number to control the SGS model dynamics.

Because of the importance of Ri in determining the SGS dynamics, a BHM based on Equation (2) for SGS turbulence will contain the likelihood distribution $[Ri_M | Ri]$, and, therefore, the deterministic skill of the method will hinge on the degree to which the model-predicted Richardson number Ri_M is an appropriate proxy for Ri . Furthermore, because Ri can be constructed in a straightforward manner from the rawinsonde data (by smoothing the measured wind and potential temperature fields to the model resolution, then evaluating the derivatives needed to compute Ri_M), we can determine *a priori* when mesoscale NWP model output is most likely to produce deterministic predictability for turbulence forecasts and when it is not.

Figure 25 shows a sample of the rawinsonde data collected during the DOE Vertical Transport and Mixing (VTMX) field program conducted in Utah's Great Salt Lake Basin. The left panel shows the potential temperature $\theta(z)$ and filtered $Ri(z)$ profiles (which we denote $Ri_\delta(z)$) for a single balloon launch. $Ri_\delta(z)$ is plotted on the right for three different filter widths δ . The shaded regions in the left panel indicate altitudes where $Ri_\delta(z) < 0.25$, with larger δ indicated by darker shading. The shaded regions identify turbulent layers, with darker layers likely more intense. Because $Ri_\delta(z)$ systematically increases with δ as a direct result of reduced gradient resolution by the coarser grid, the higher- δ profiles predict many fewer active mixing layers than are actually present. This is significant because the coarsest filter width used $\delta=300\text{m}$, typical of mesoscale-model vertical

resolutions, explicitly demonstrates that NWP models based on current common practices alone cannot possibly predict but a small fraction of the dynamical layers that naturally occur in stratified environments; hence, it is the case that conventional NWP model output must be integrated with other data sources to exhibit predictive power when attempting to forecast atmospheric turbulence.

The right panels in Figure 25 show normalized PDFs for Ri , i.e., $[Ri]$ for the troposphere and stratosphere combined. The top panel shows the results from a single balloon launch, with four sets of data indicated for each of four filter widths. The data in the bottom panel results after combining data for 82 separate balloon flights; note the much smoother profiles and clear systematic dependence on δ for the larger statistical sample. As with the other PDFs examined, the normalized Ri PDFs exhibit a universal shape and can therefore be characterized solely by their mean and RMS values.

Figure 26 examines the conditional probability density $[Ri_M | Ri]$, estimated from the rawinsonde measurements, by presenting the mean and RMS of the ensemble PDF's presented in the lower-right panel of Figure 25. Figure 26 shows results for the same filter widths δ used in constructing Figure 25. It is apparent that as δ is increased, the relationship between the mean and RMS predicted values for Ri_δ and the actual value Ri becomes weaker, i.e., the curves become flatter. When the curves are completely flat, fidelity from the procedure to predict mean and RMS values is lost, and the estimated $[Ri_M | Ri]$ distribution becomes identical to that predicted by a regional climatology model for Ri based on archived rawinsonde data. We note that this appears to occur at all of the rawinsonde launch sites at VTMX and CASES-99 at a resolution of about 300m. Hence, in order to obtain high-fidelity Ri predictions from model data, NWP models must achieve greater resolution than they do currently, and the evaluated Ri_M measures currently used in stability-corrected mixing-length applications undoubtedly relate poorly to the actual values that should be used. Clearly a BHM approach would significantly improve the situation, and given the apparent universal form of the ensemble PDFs in the lower-right panel of Figure 25, Ri climatologies appear to be feasible. This is excellent news for BHM methods applied to regions where sparse or no current data is available, but for which compilations of representative PDFs are possible, either through available archived results or via results for a dynamically similar surrogate region.

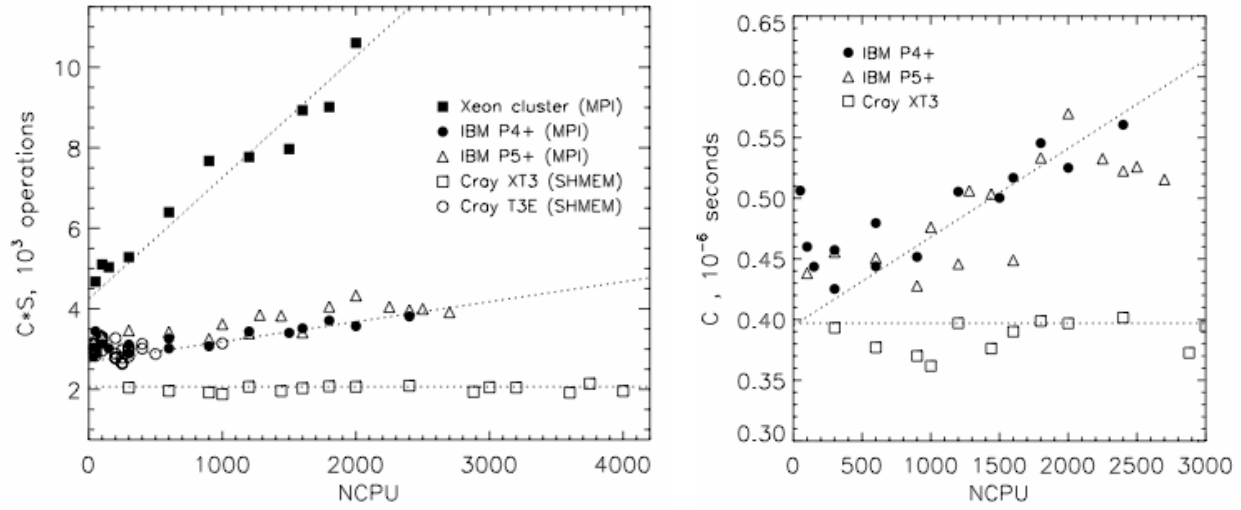


Figure 1. *Parallel performance on five supercomputer platforms. C is proportional to the wall time per compute cycle; S is the peak processor speed. Left panel shows $C \cdot S$, which isolates the inter-processor network performance. Asymptotic fits to the XT3, P4+ and Xeon data are shown (dotted lines). SHMEM or MPI communication libraries are used, depending on which is fastest. Right panel shows C alone, which indicates the relative wall-clock time to complete an operation on three of the platforms. For certain NCPU (e.g., 900, 1200 and 1600), the P5+ and XT3 times are within $\approx 10\%$ of each other.*



Figure 2. *Vorticity in stratified wind shear for $Ri=0.15$ showing large range of length scales present. The ratio of sizes for the largest and smallest eddies is roughly 150. Given that 5 to 8 grid points are required to resolve the smallest eddies, it is clear that very large numerical meshes are required to simulate such flows with DNS. Only two of the four large-scale billows simulated are shown so that small-scale features can be viewed. Layer Reynolds numbers of $Re \geq 30,000$ are required to achieve sufficient scale separation to be atmospherically relevant, while four billows are needed to obtain adequate statistics to populate the probability density functions needed for the BHM approach employed..*

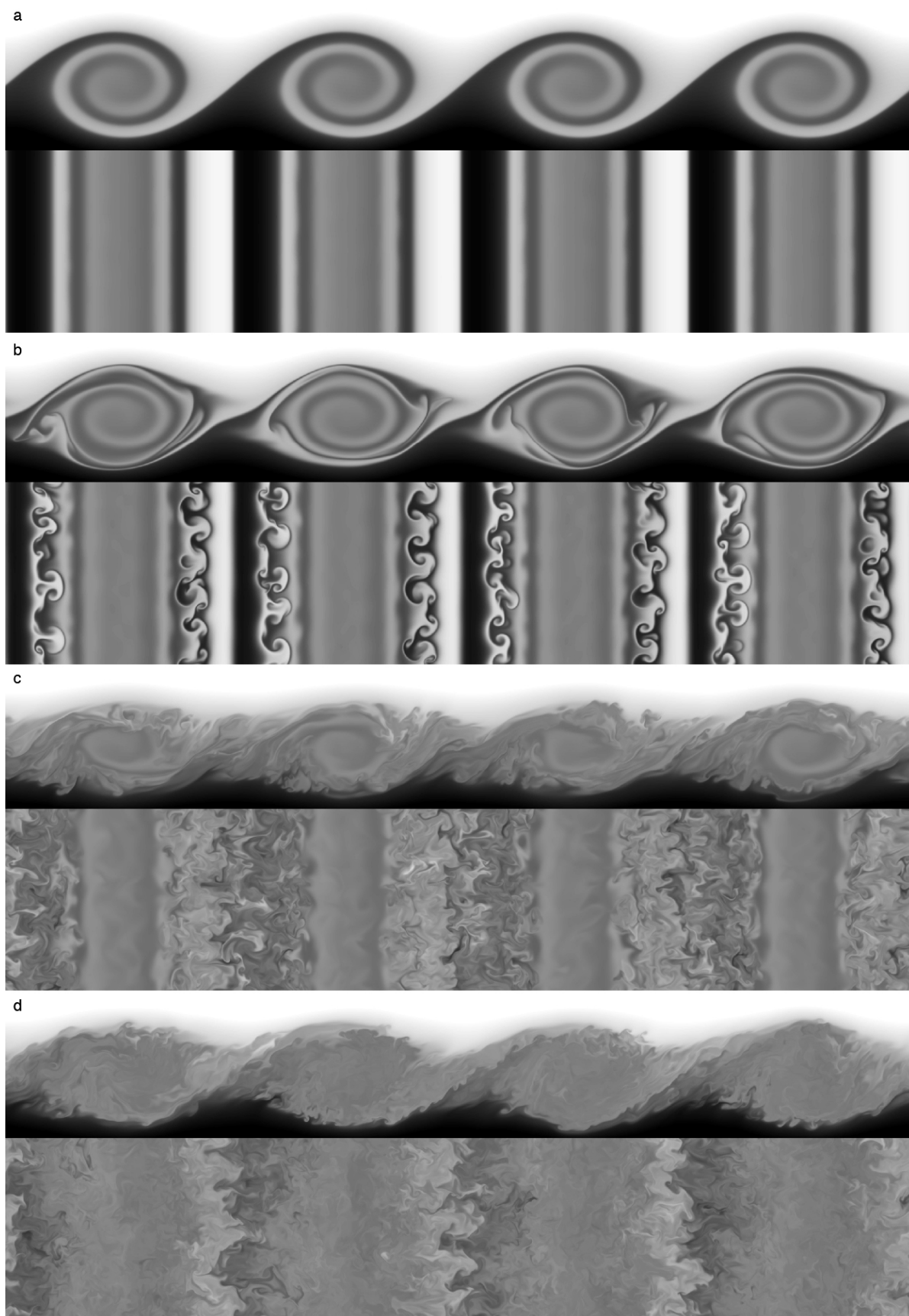


Figure 3. (Continued next page.)

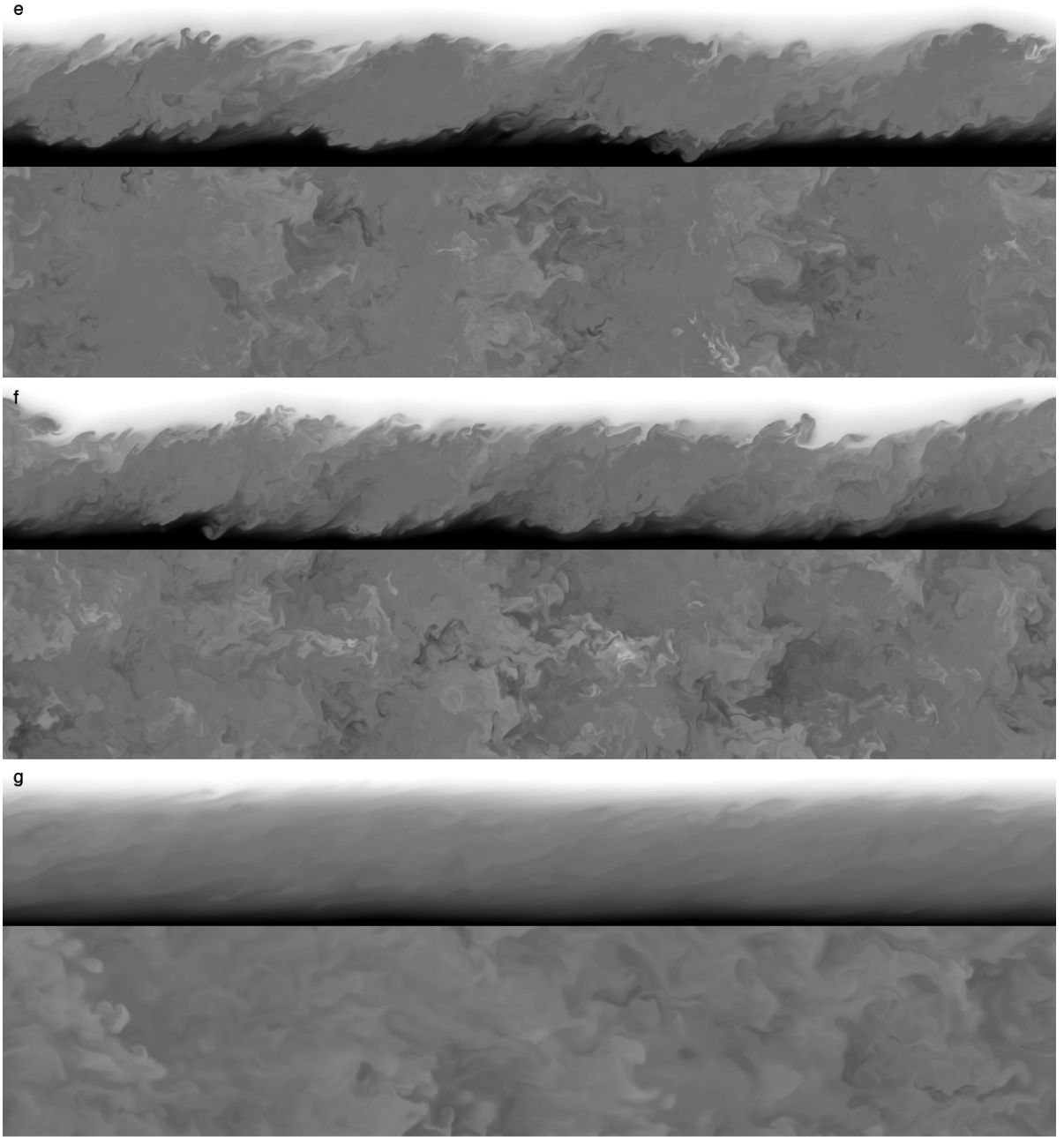


Figure 3. *Temperature in stratified wind shear for $Ri=0.05$ and $Re=2500$ at seven distinct times during the flow evolution. For each time, two panels are shown: 1) a side view of the four billows and 2) a top view of 40% of the mid-plane. The times chosen correspond to when (a) billows reach maximum amplitude, $t=37$; (b) secondary instability triggers the transition to turbulence, $t=54$; (c) KE and PE dip to local minima before secondary peaks in KE and PE occur, $t=68$; (d) KE and PE exhibit secondary maxima, $t=85$; (e) turbulence intensity and vorticity magnitude attain maximum values, coincident with a local minimum in PE, $t=111$, (f) turbulence first becomes horizontally homogeneous, $t=130$; and (g) turbulence decay exhibits a change in character, $t=251$. Panels a-d appear on the preceding page.*

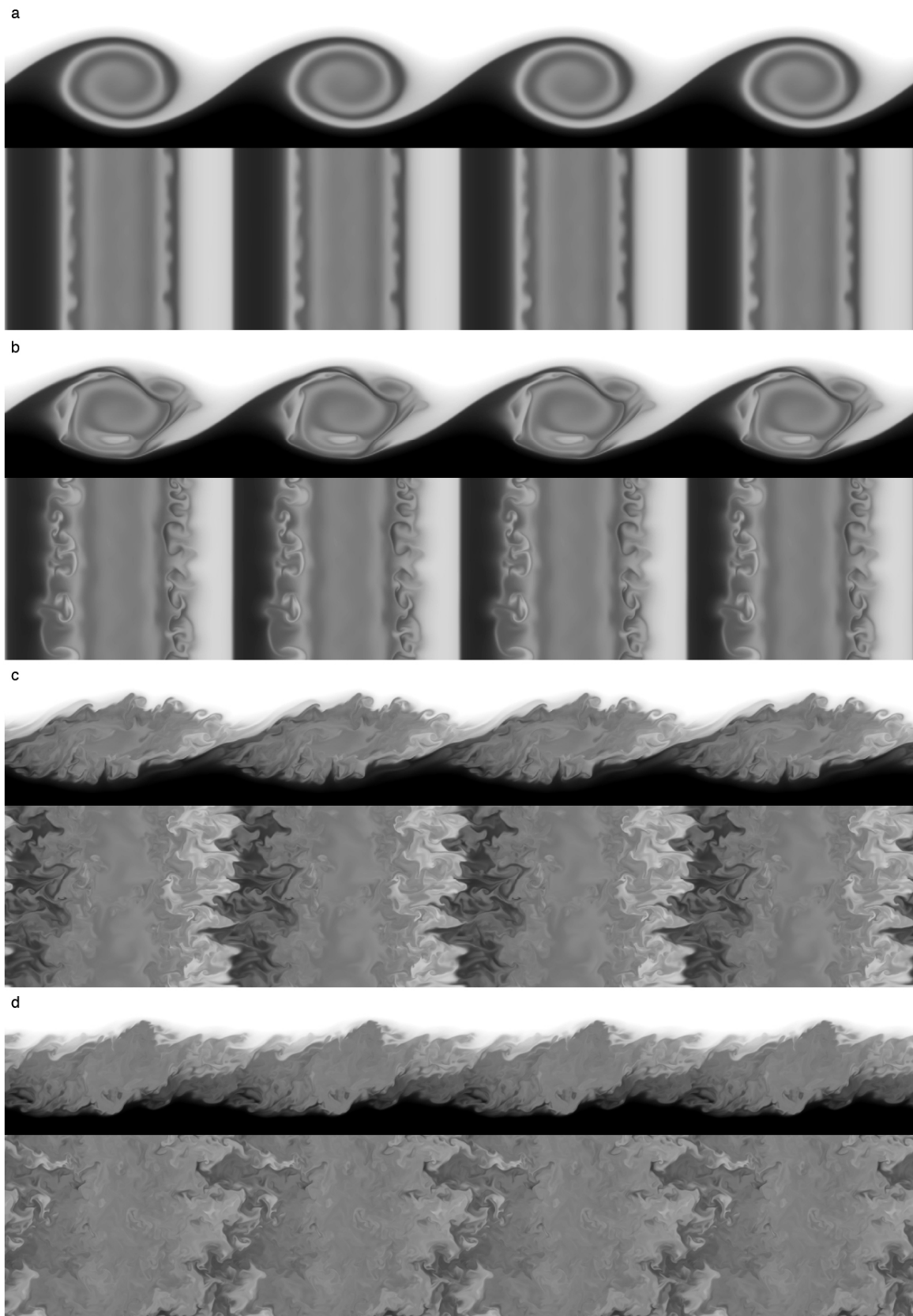


Figure 4. (Continued next page.)

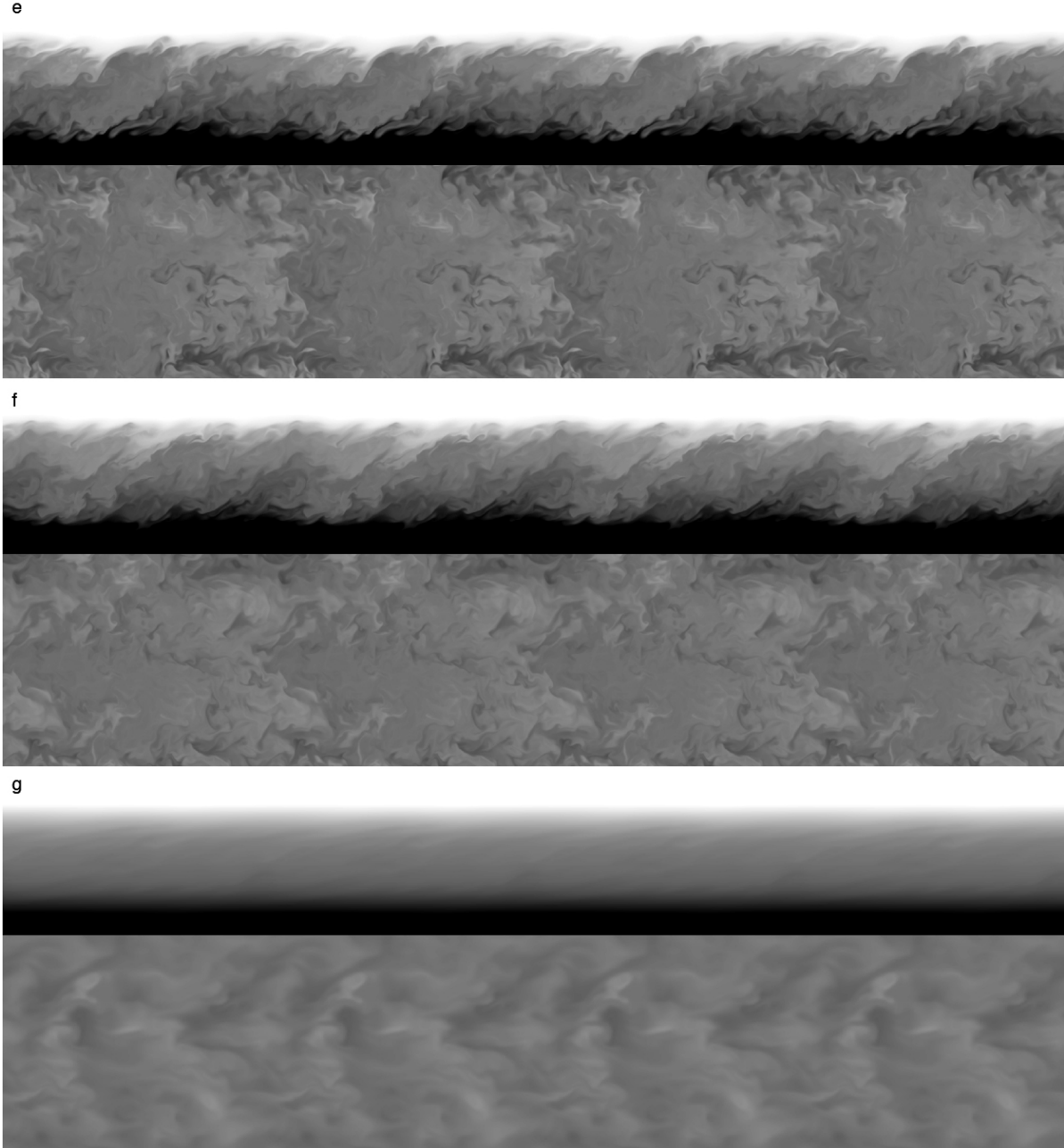


Figure 4. *Temperature in stratified wind shear for $Ri=0.10$ and $Re=2500$. Seven times are presented, as in Figure 3, but because the evolution depends strongly on Ri , some of the times correspond to different stages in the flow evolution and morphology. Times chosen correspond to when (a) billows reach maximum amplitude, $t=44$; (b) secondary instability appears in the billow edge region, $t=54$; (c) turbulence intensifies in billow edges and reaches braids, $t=68$; (d) turbulence peaks in the billow cores, $t=76$; (e) vorticity magnitude attains maximum, coincident with a local minimum in PE, $t=89$, (f) turbulence first becomes horizontally homogeneous, $t=97$; and (g) turbulence decay exhibits a change in character, $t=165$. Panels a-d appear on the preceding page. Note: this solution is only of a single billow which has been replicated to be consistent with Figures 3, 5, and 6.*

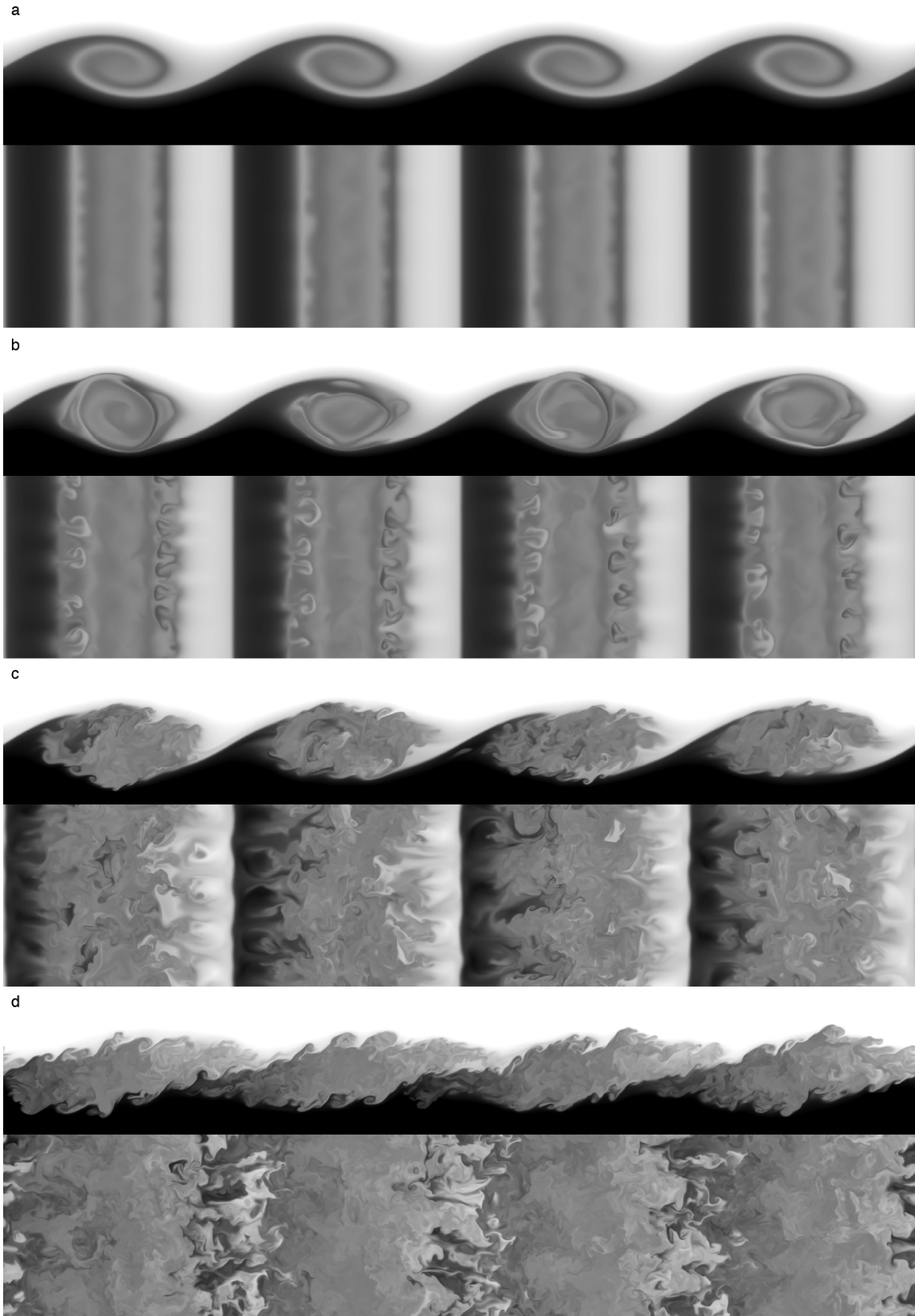


Figure 5. (Continued next page.)

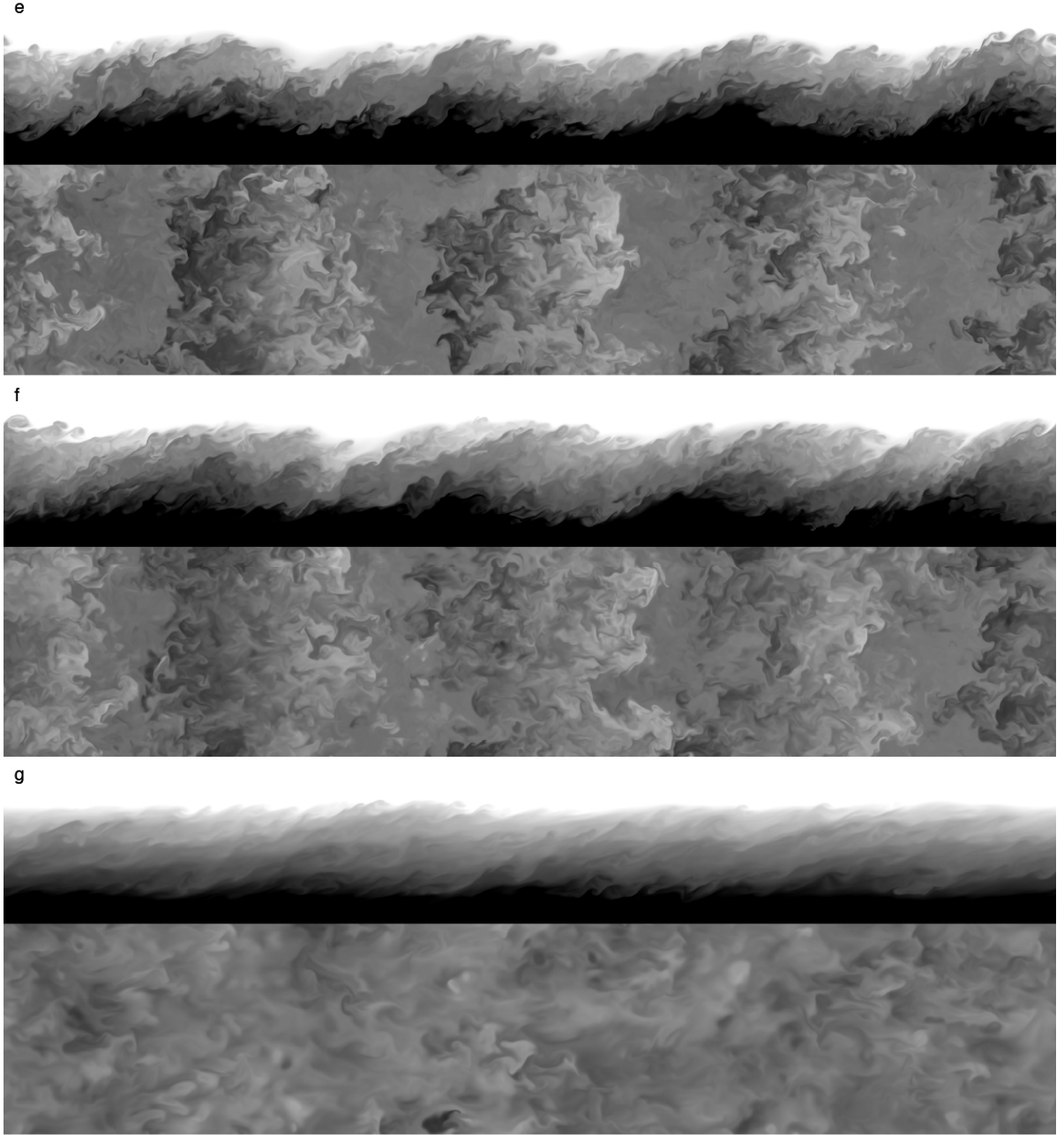


Figure 5. *Temperature in stratified wind shear for $Ri=0.15$ and $Re=2900$. Seven times are presented. Times chosen correspond to when (a) billows reach maximum laminar amplitude, $t=44$; (b) billows reach maximum amplitude, with instability developing in the billow edge region, also coincident with maximum PE, $t=57$; (c) turbulence invades billow cores, $t=67$; (d) turbulence reaches braids, $t=77$; (e) turbulence begins exponential decay phase, $t=86$; (f) turbulence first becomes horizontally homogeneous, $t=91$; and (g) turbulence decay exhibits a change in character, $t=116$. Panels a-d appear on the preceding page.*

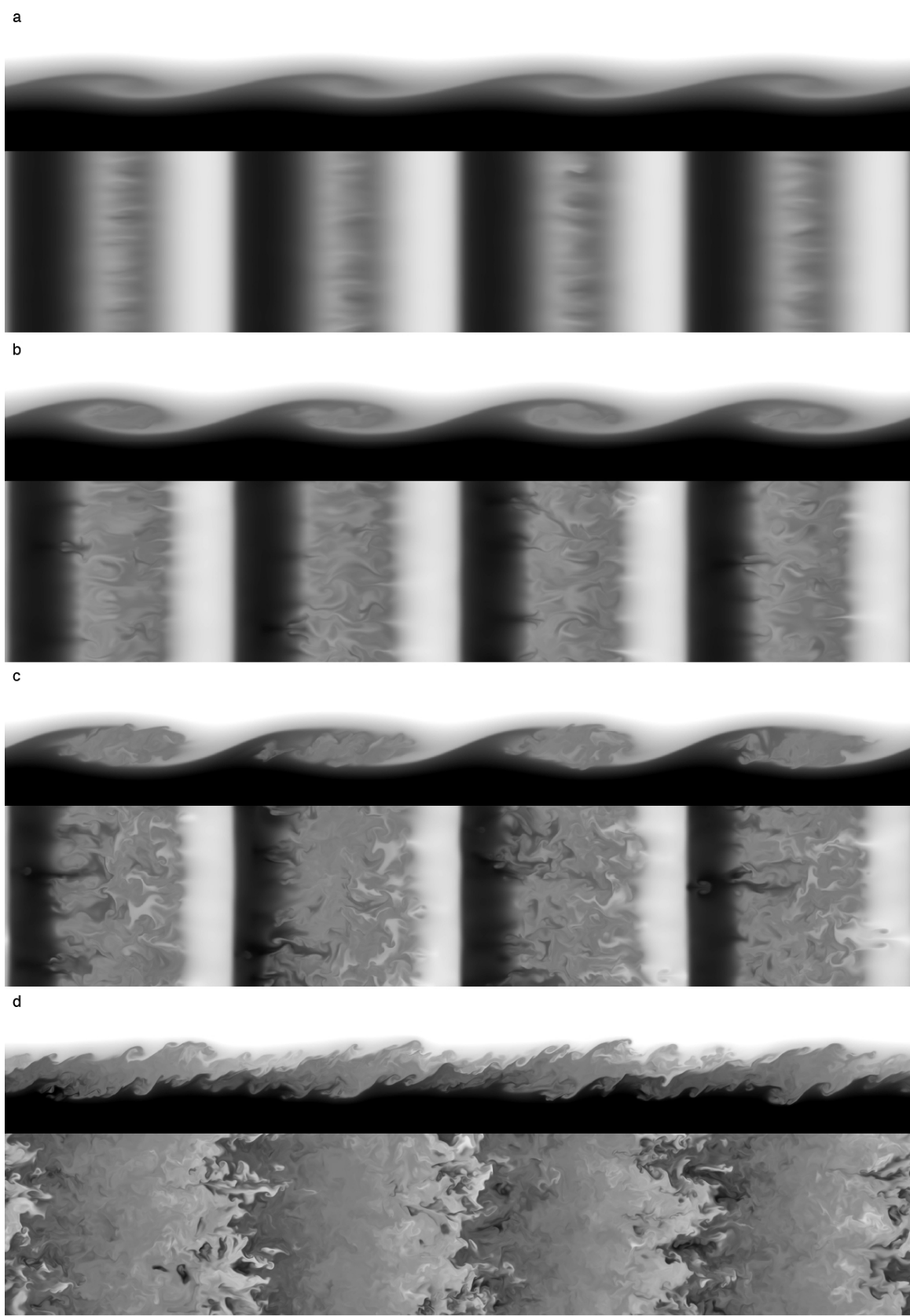


Figure 6. (Continued next page.)

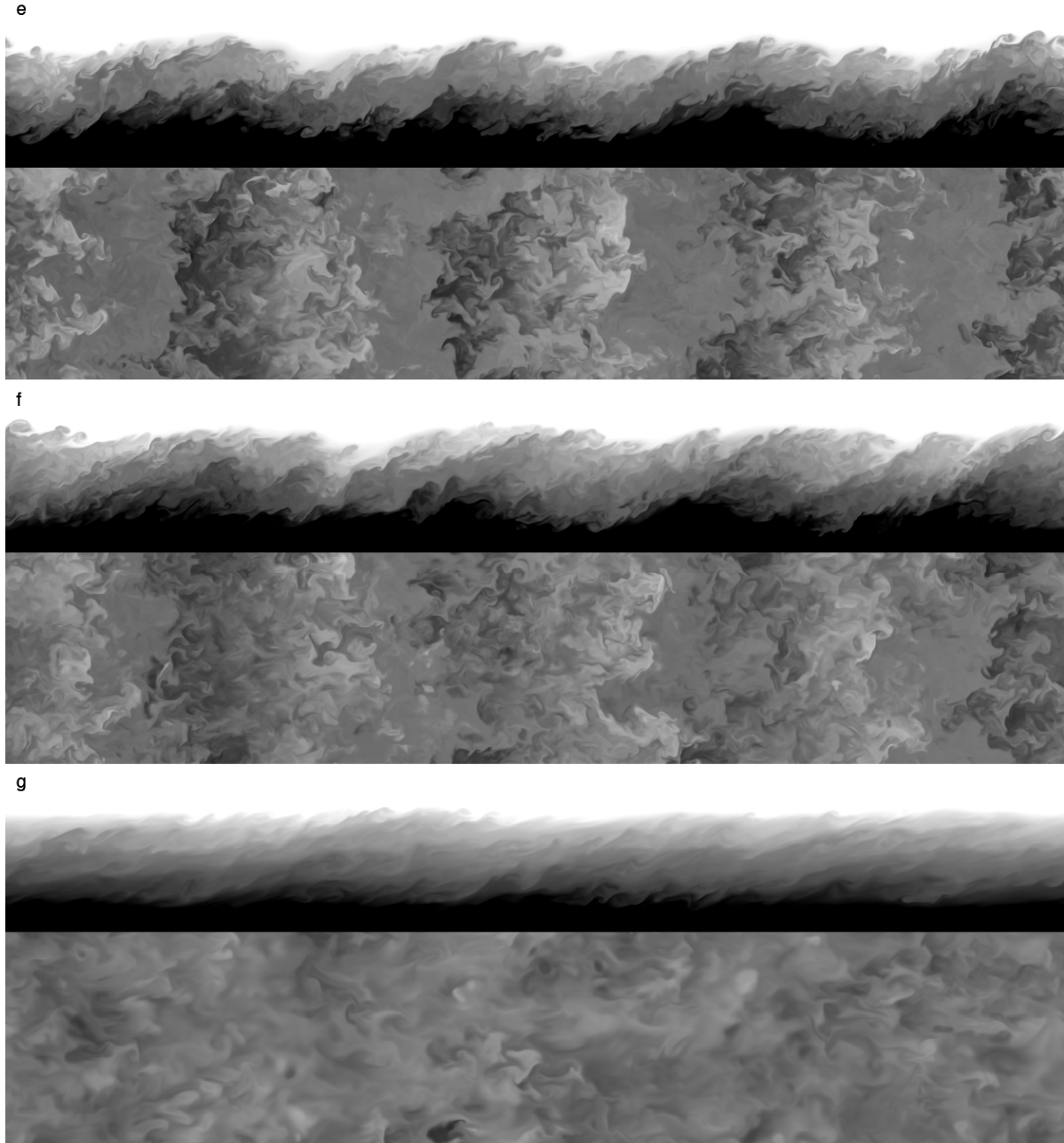


Figure 6. *Temperature in stratified wind shear for $Ri=0.20$ and $Re=4000$. Seven times are presented. Times chosen correspond to when (a) billows reach maximum laminar amplitude, $t=37$; (b) billows reach maximum amplitude, with turbulence erupting in the billow cores, $t=54$; (c) PE peaks, $t=66$; (d) turbulence reaches braids, $t=82$; (e) turbulence begins exponential decay, $t=90$; (f) turbulence first becomes horizontally homogeneous, $t=105$; and (g) turbulence late in the exponential decay phase, $t=130$. Panels a-d appear on the preceding page.*

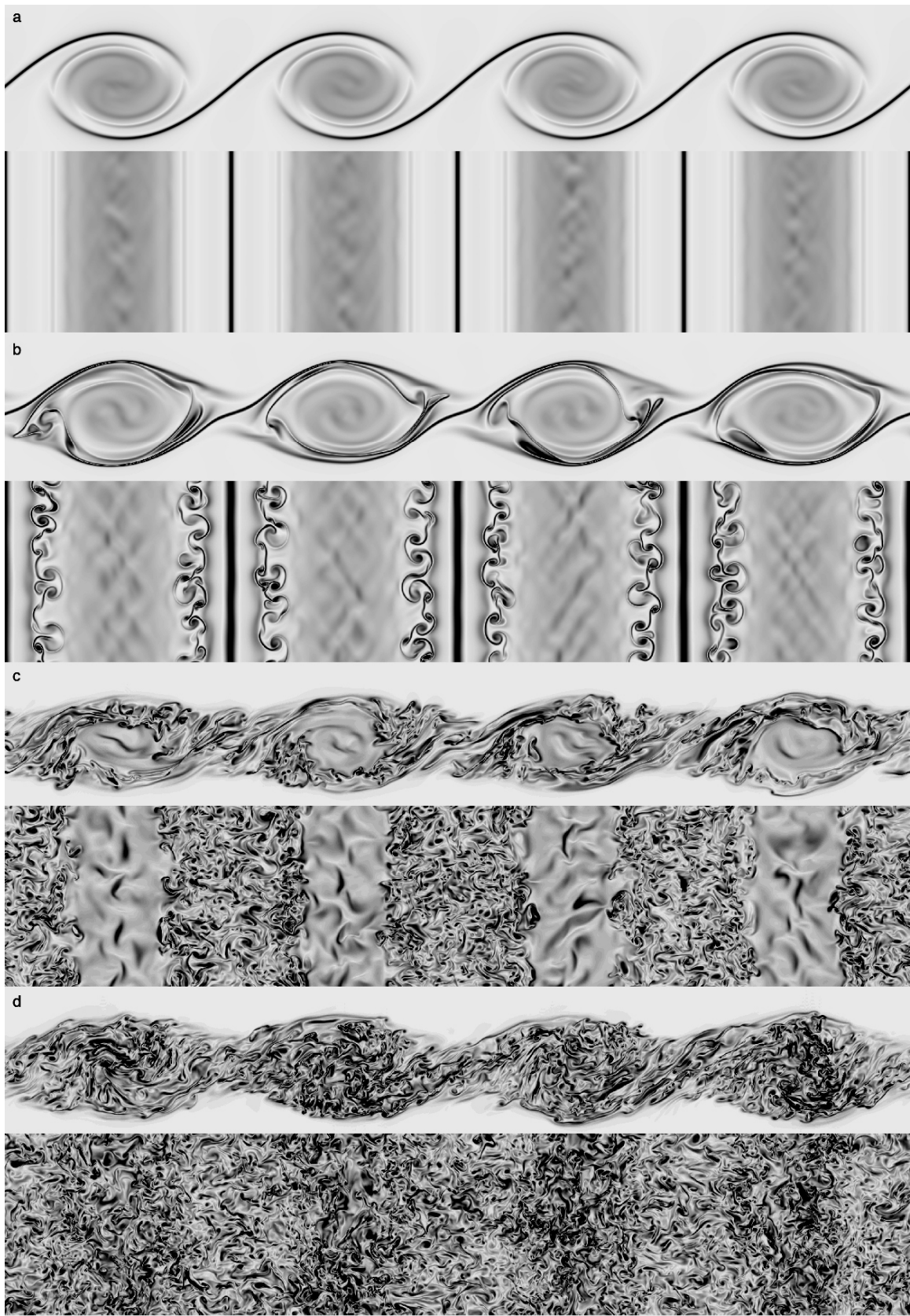


Figure 7. (Continued next page.)

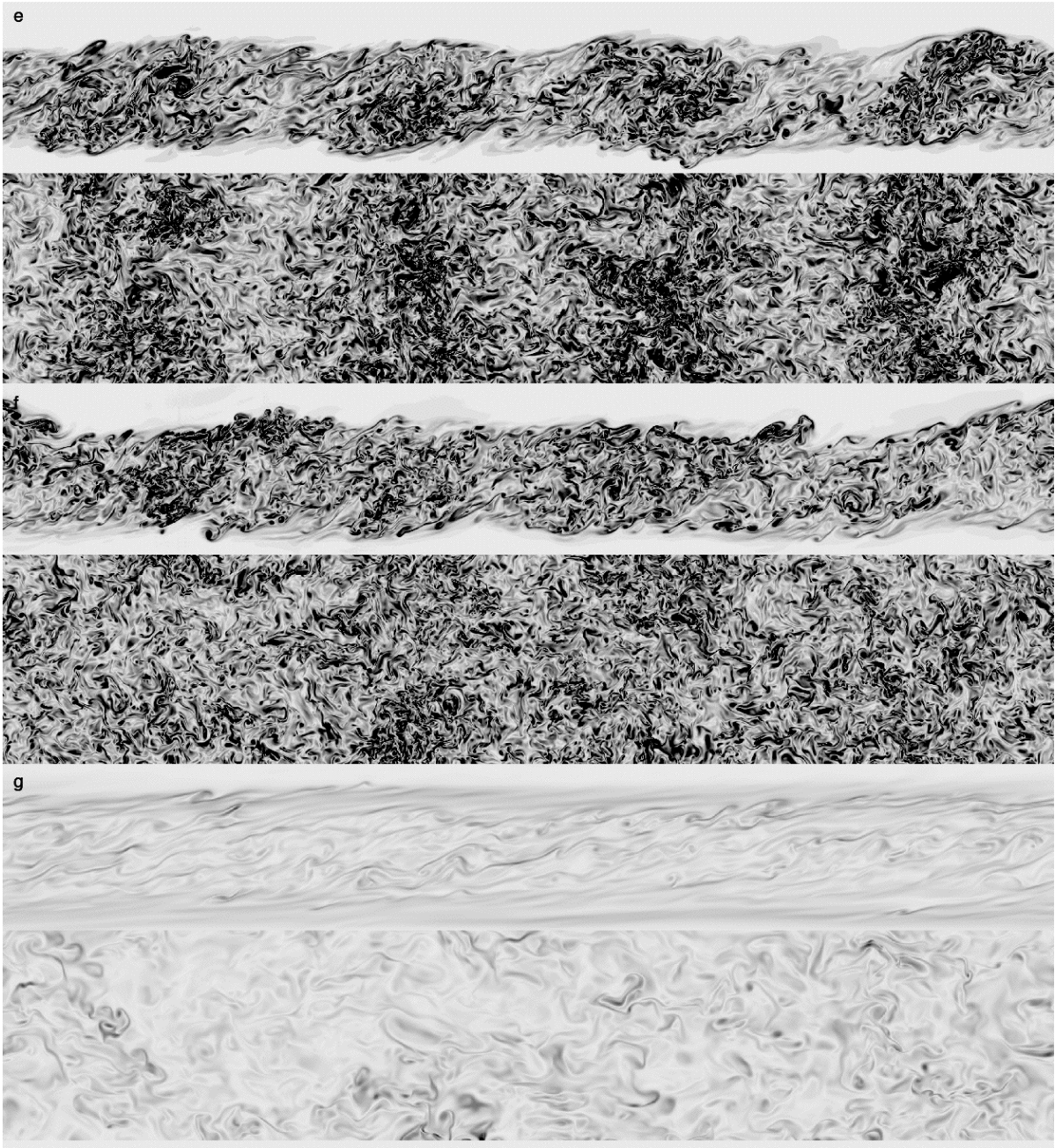


Figure 7. *Vorticity magnitude in stratified wind shear for $Ri=0.05$ and $Re=2500$. Panels a-d appear on the preceding page. See Figure 3's caption for times associated with each panel.*

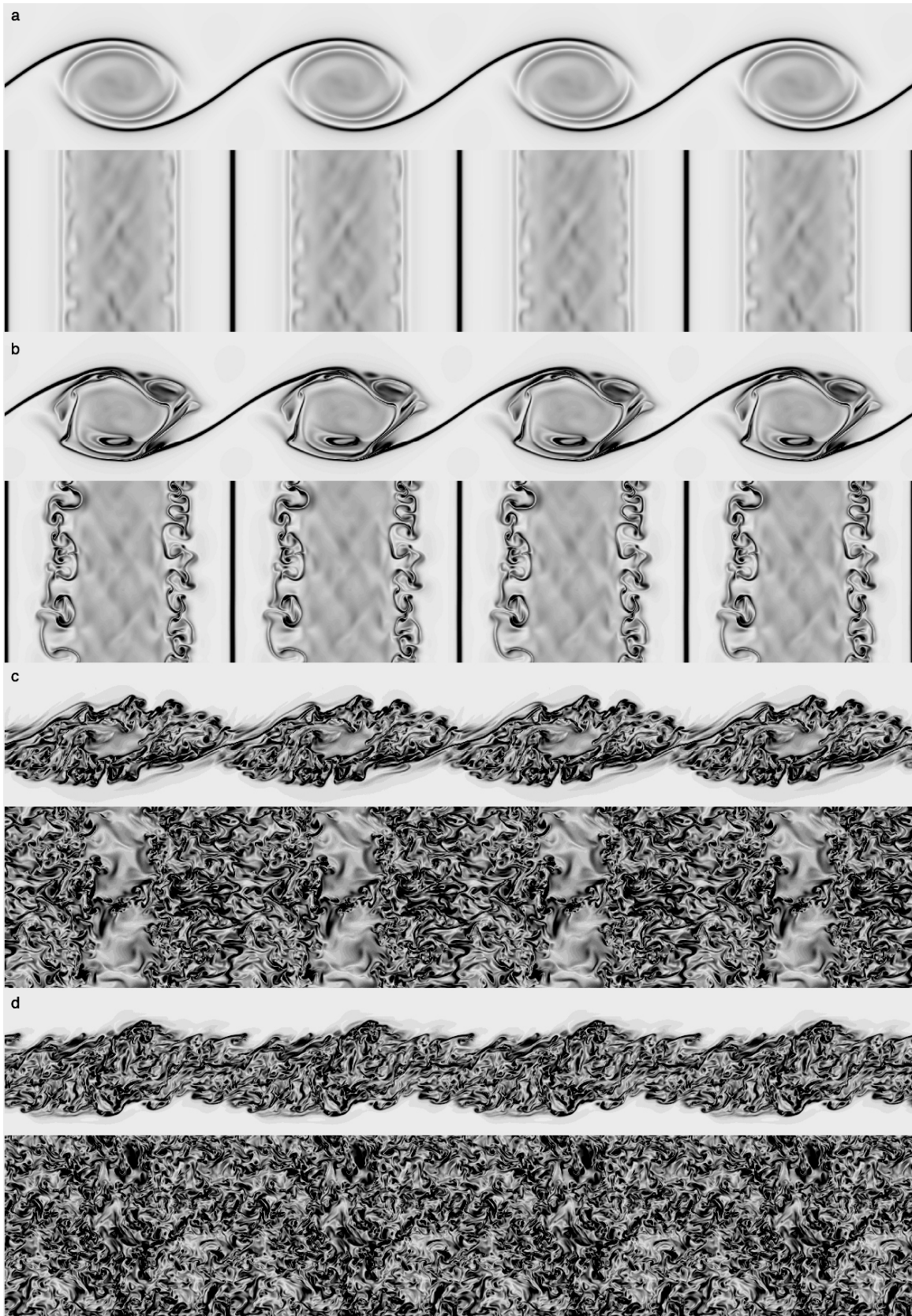


Figure 8. (Continued next page.)

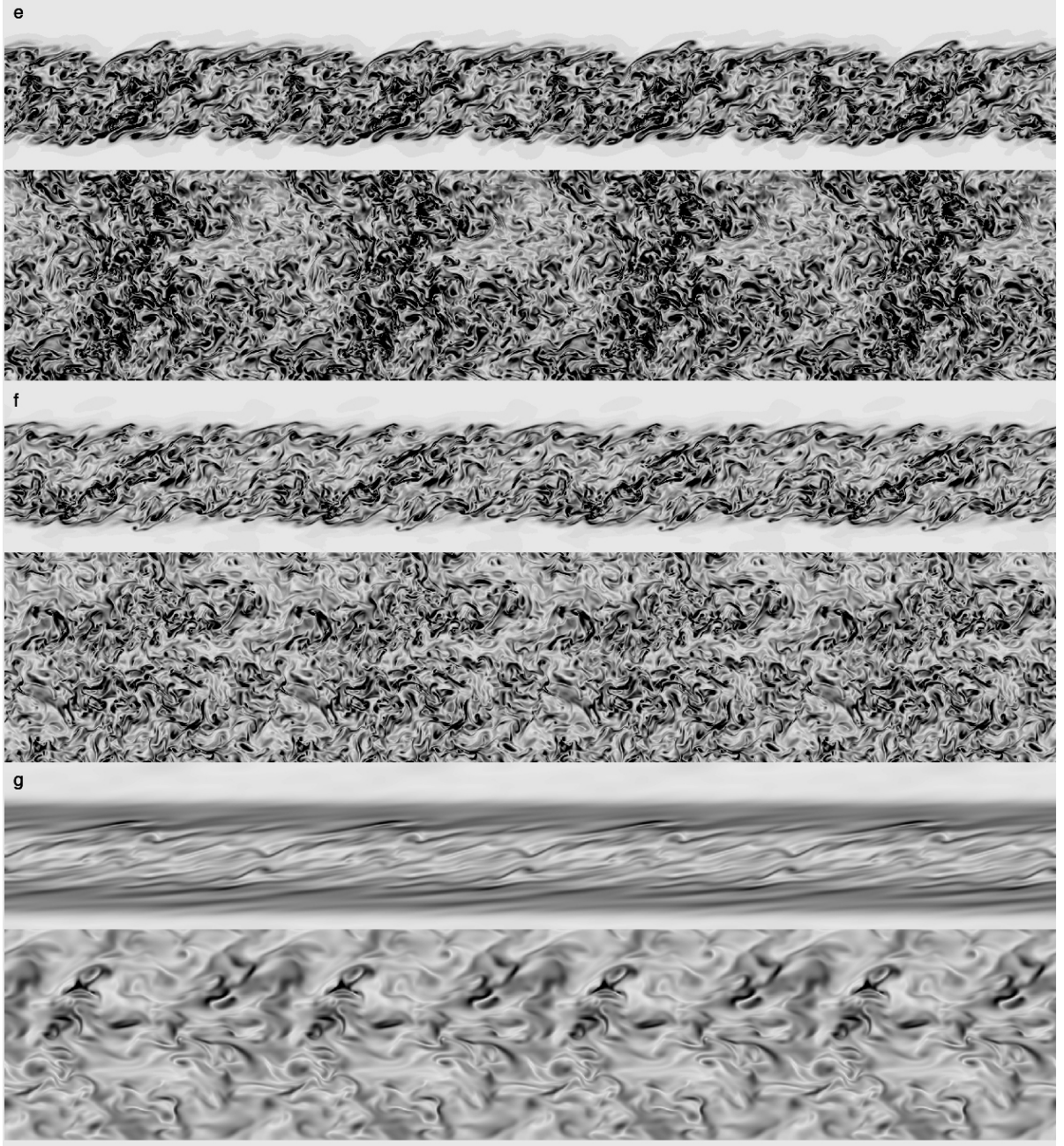


Figure 8. *Vorticity magnitude in stratified wind shear for $Ri=0.10$ and $Re=2500$. Panels a-d appear on the preceding page. See Figure 4's caption for times associated with each panel. Note: this solution is only of a single billow that has been replicated to be consistent with Figures 7, 9, and 10.*

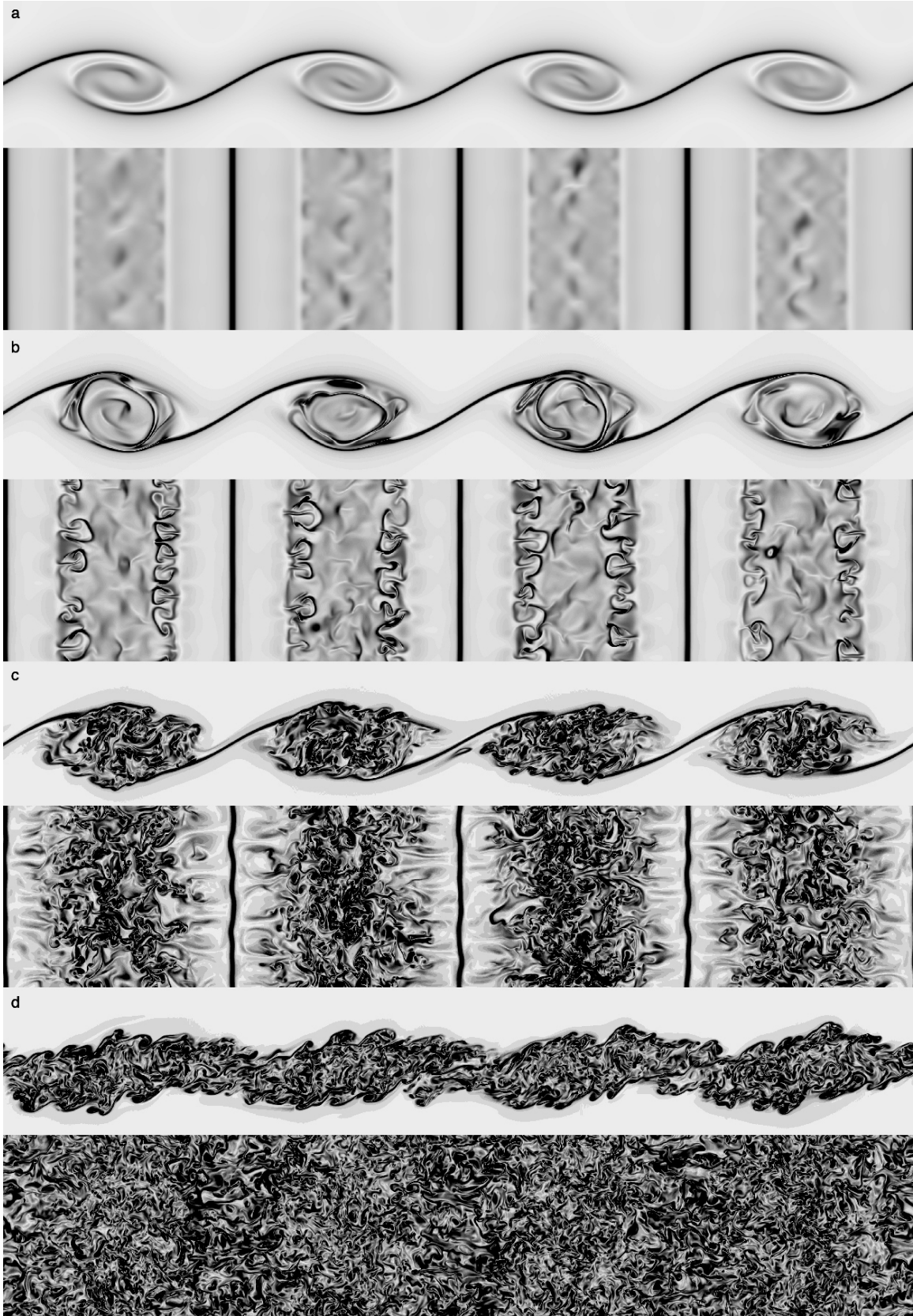


Figure 9. (Continued next page.)

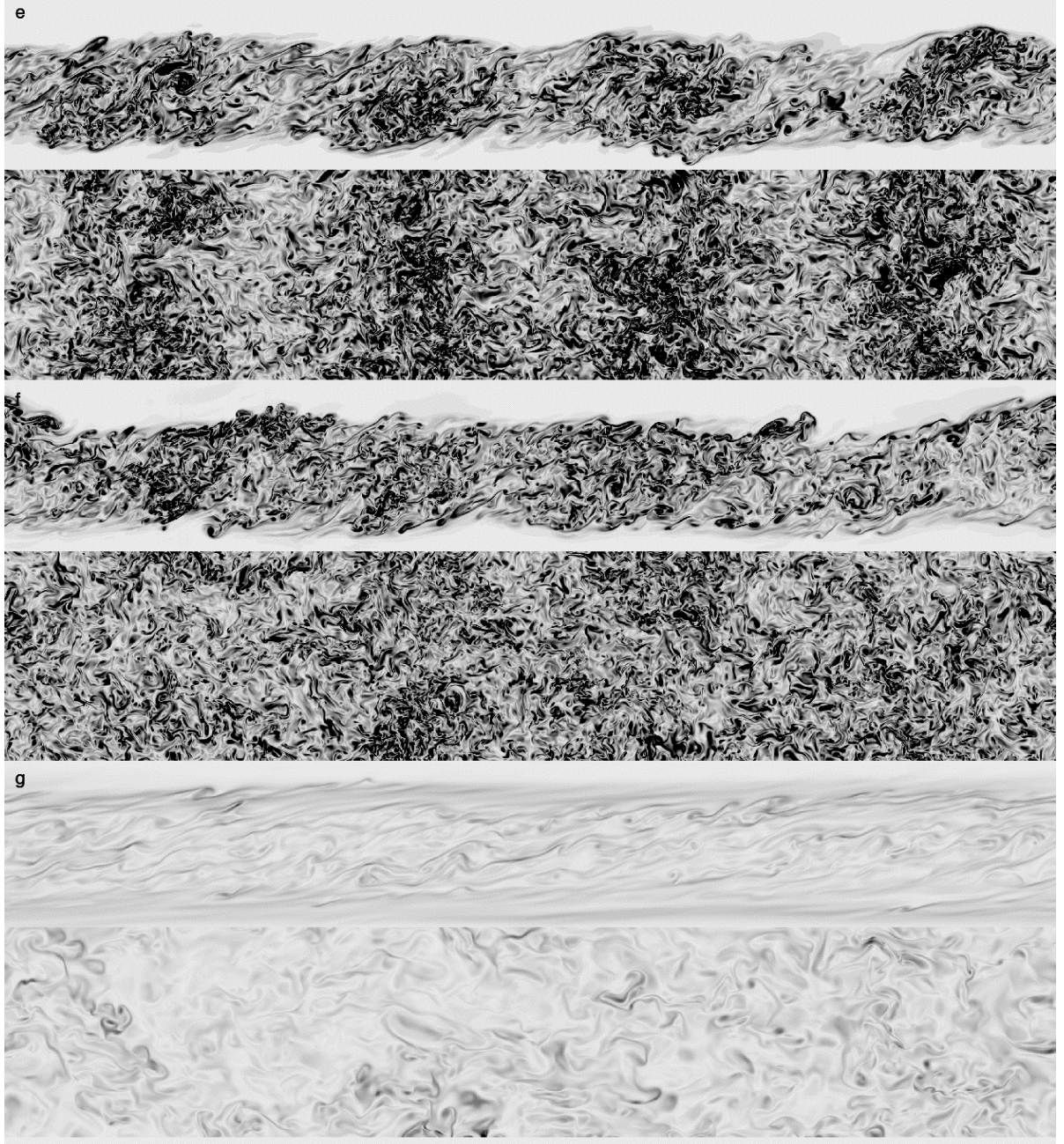


Figure 9. *Vorticity magnitude in stratified wind shear for $Ri=0.15$ and $Re=2900$. Panels a-d appear on the preceding page. See Figure 5's caption for times associated with each panel.*

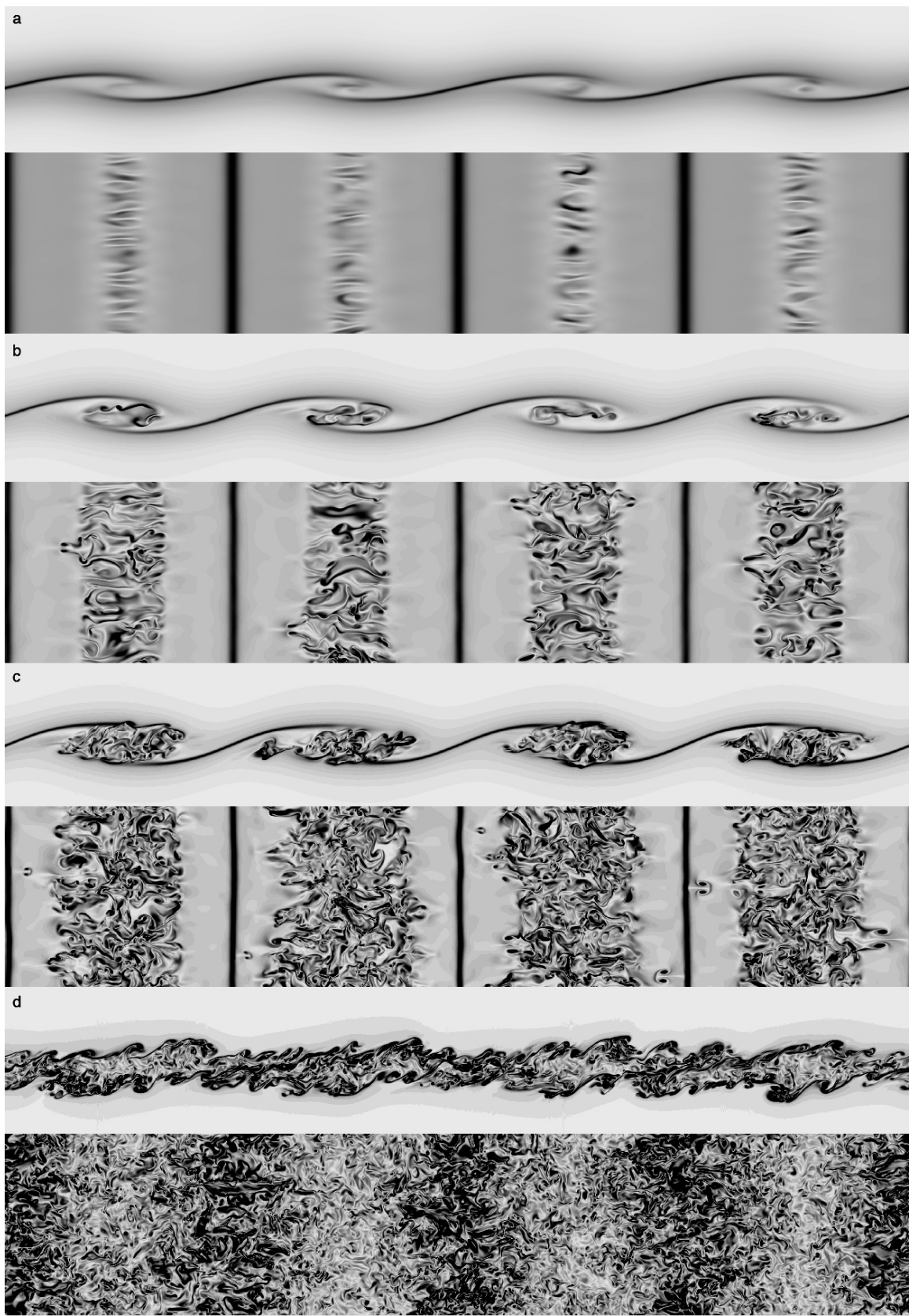


Figure 10. (Continued next page.)

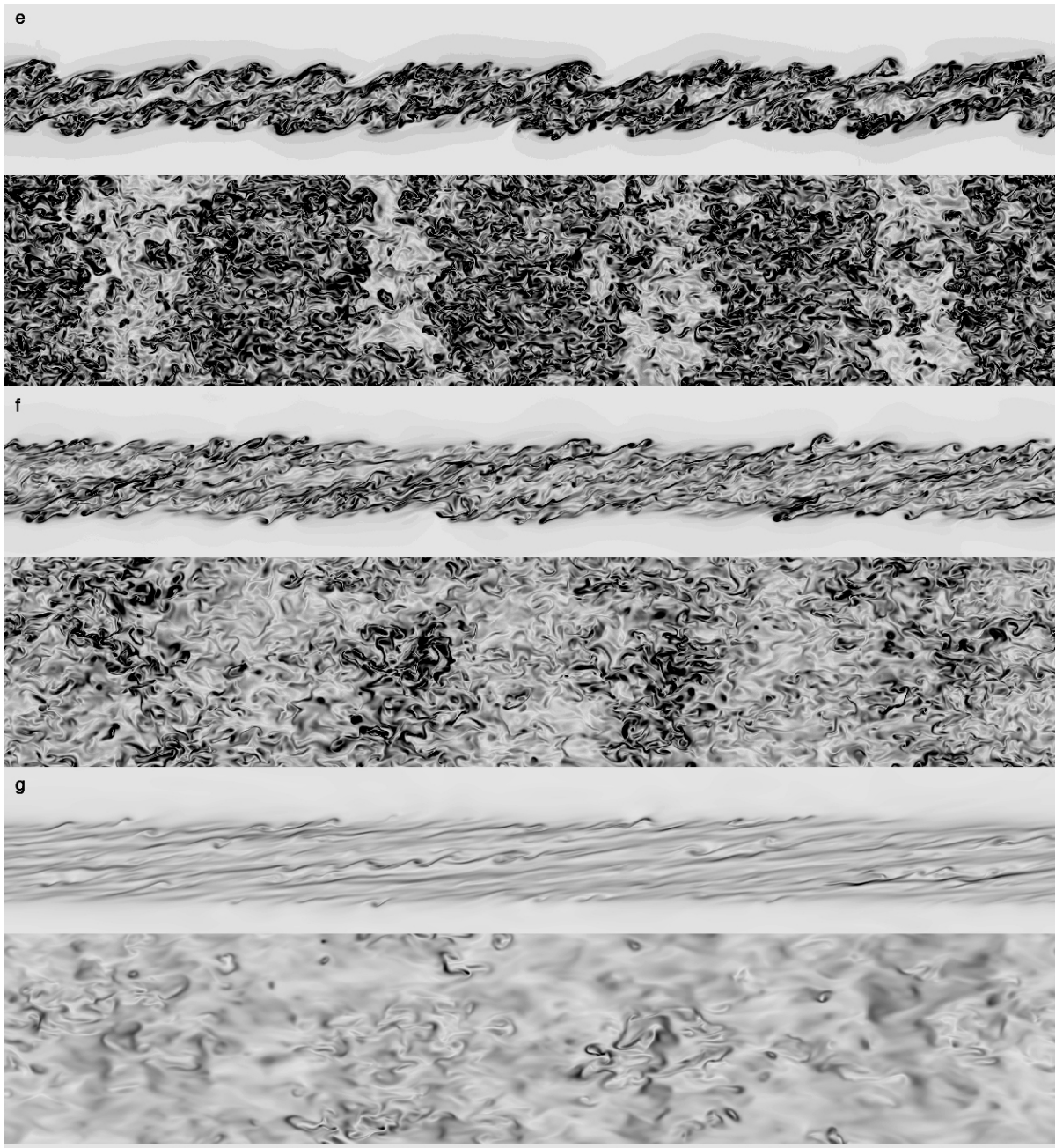


Figure 10. *Vorticity magnitude in stratified wind shear for $Ri=0.20$ and $Re=4000$. Panels a-d appear on the preceding page. See Figure 6's caption for times associated with each panel.*

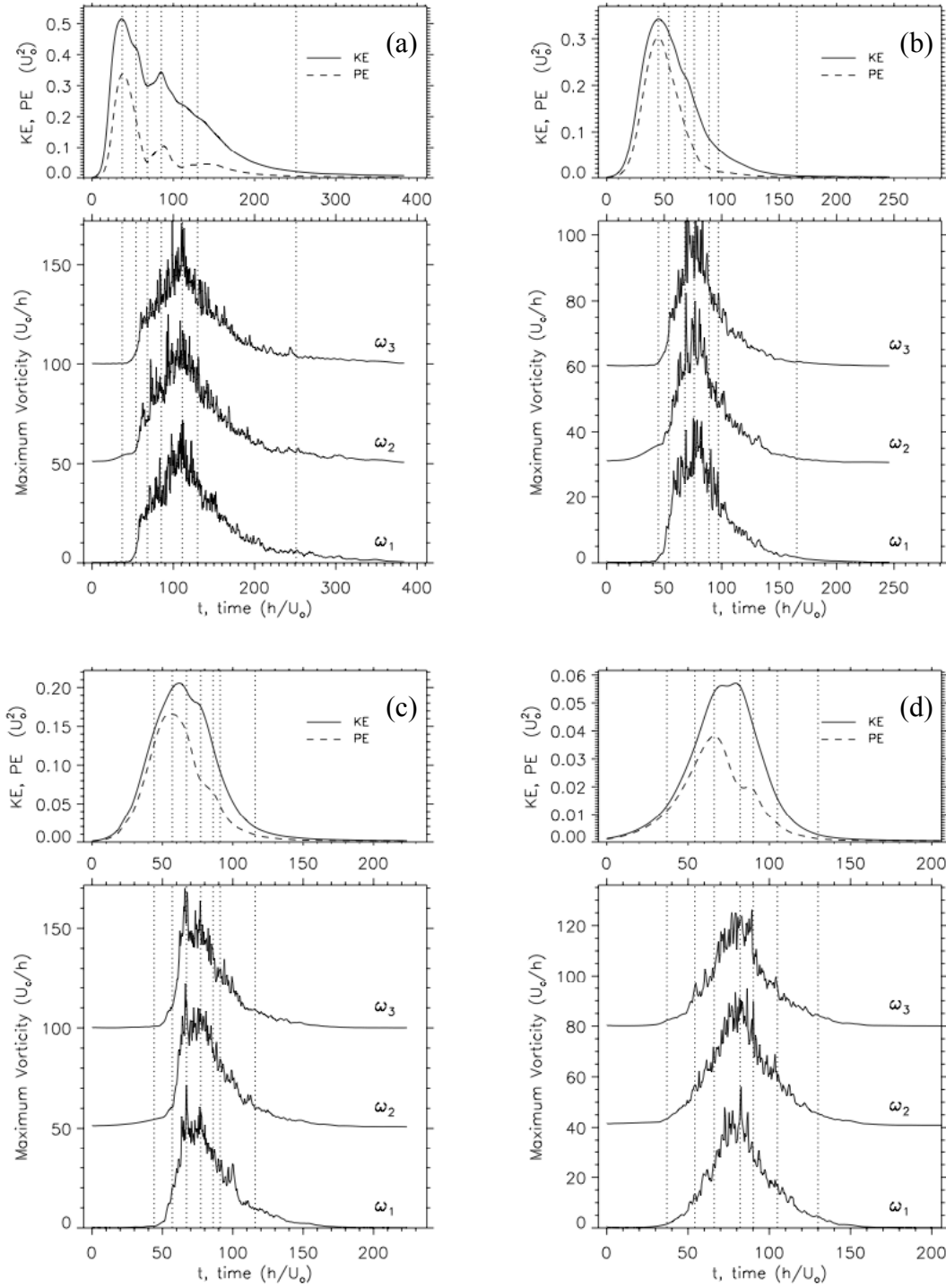


Figure 11 Time evolution of fluctuation kinetic energy KE (solid line) and an estimate for the potential energy PE (dashed line) (top panels) and the maximum of each vorticity component (bottom panels) for (a) $Ri=0.05$, (b) $Ri=0.10$, (c) $Ri=0.15$, and (d) $Ri=0.20$. Vertical dotted lines correspond to the times shown in Figures 3-10.

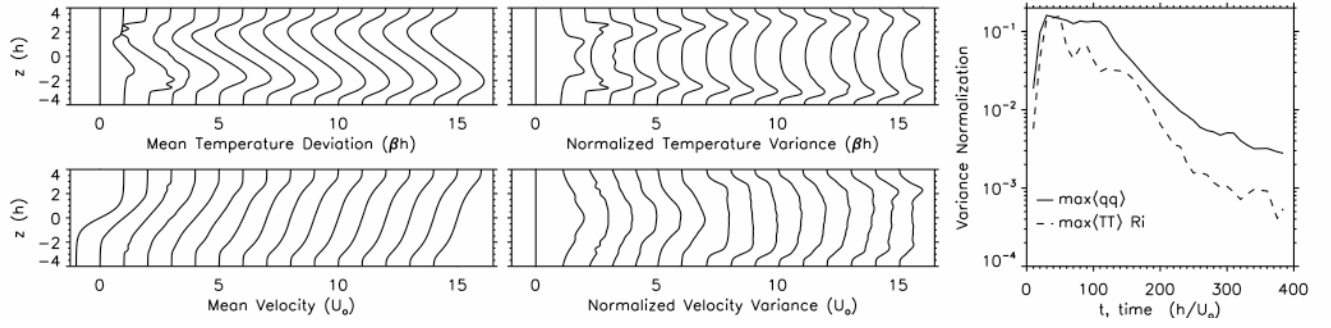


Figure 12. $Ri=0.05$ – Horizontally averaged profiles for the mean temperature (upper left) and mean streamwise velocity (lower left) and for the normalized temperature variance (upper middle) and normalized velocity variance (lower middle). The variance normalization factors used in the middle panels are shown in the rightmost panel. The solid (dashed) curve depicts the velocity variance $\langle q^2 \rangle = \langle u^2 + v^2 + w^2 \rangle$ (temperature variance $\langle T^2 \rangle$).

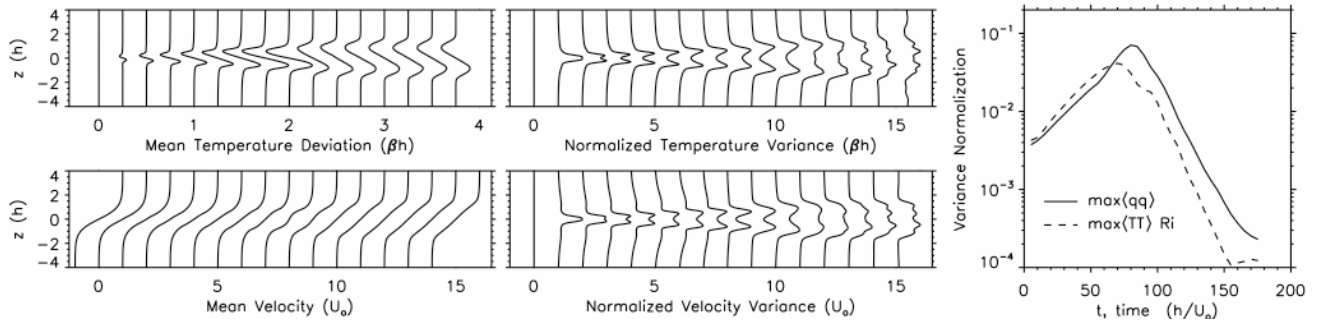


Figure 13. $Ri=0.20$ – Horizontally averaged profiles for the mean temperature (upper left) and mean streamwise velocity (lower left) and for the normalized temperature variance (upper middle) and normalized velocity variance (lower middle). The variance normalization factors used in the middle panels are shown in the rightmost panel. The solid (dashed) curve depicts the velocity variance $\langle q^2 \rangle = \langle u^2 + v^2 + w^2 \rangle$ (temperature variance $\langle T^2 \rangle$).

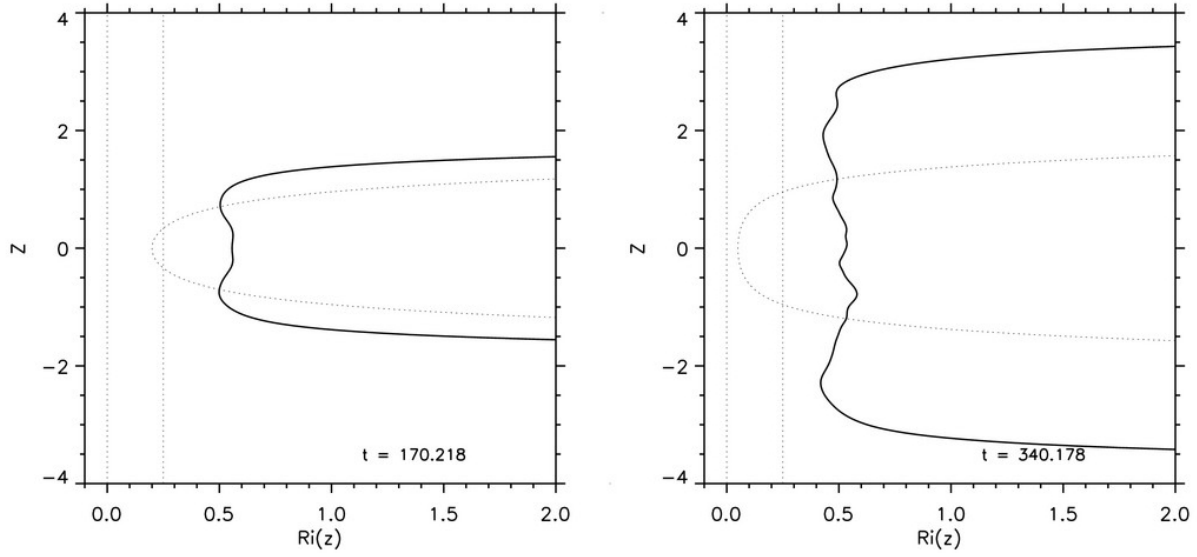


Figure 14. $Ri(z)$ profiles for wind-shear simulations with $Ri=0.20$ (left) and $Ri=0.05$ (right). Initial (dotted) and final (solid) profiles are shown. The time of the final profile is selected at late time during final restratification.

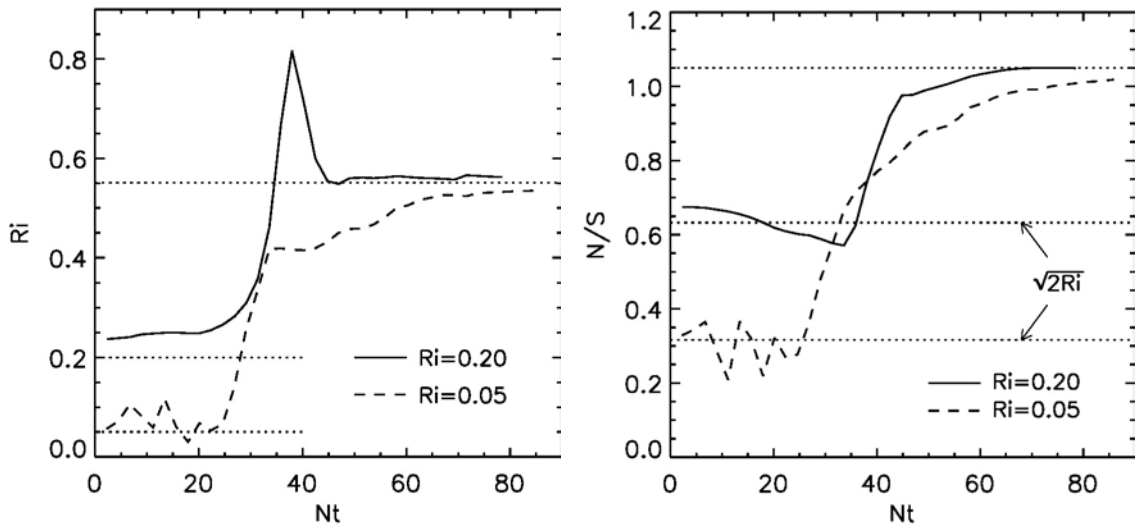


Figure 15. Mid-layer Richardson number $Ri(0)$ (left panel) and N/S (right panel) versus Nt for $Ri=0.05$ (dashed) and $Ri=0.20$ (solid). $Ri(0)$ results from averaging $Ri(z)$ from $z=-0.5$ to $z=0.5$. See text for definition of S .

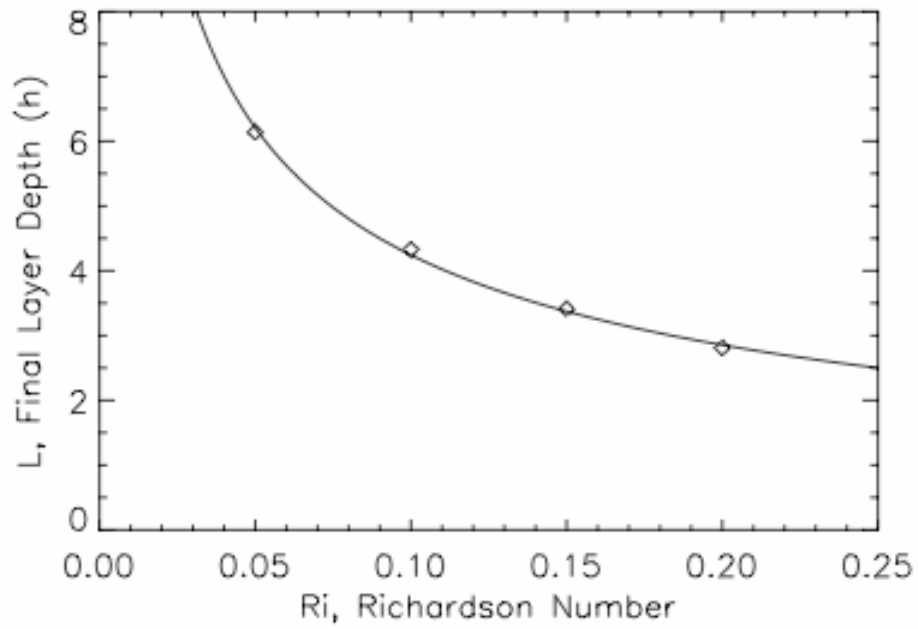


Figure 16. *Final layer depth L versus initial layer Richardson number Ri for four wind-shear simulations. Data points show the simulation results, while the solid curve is a fit of the form $L=1.5 Ri^{-1/2} - 0.05$.*

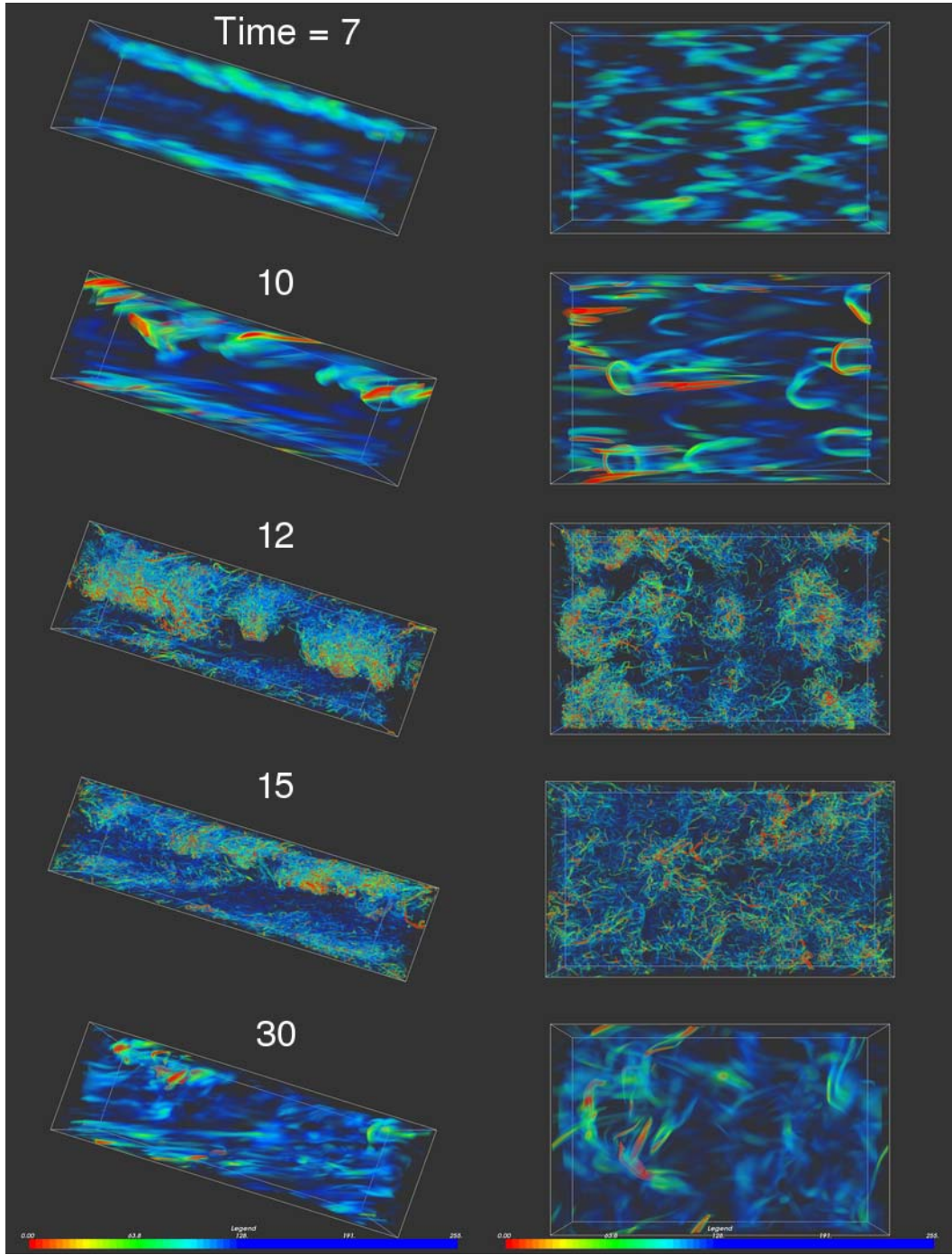


Figure 17. 3D evolution of vortex tubes (λ_2 visualization) for an amplitude $A=1.1$ gravity wave viewed from the side and from above. Red and yellow regions denote the most intense rotation. Wave propagation is to the left in all panels.

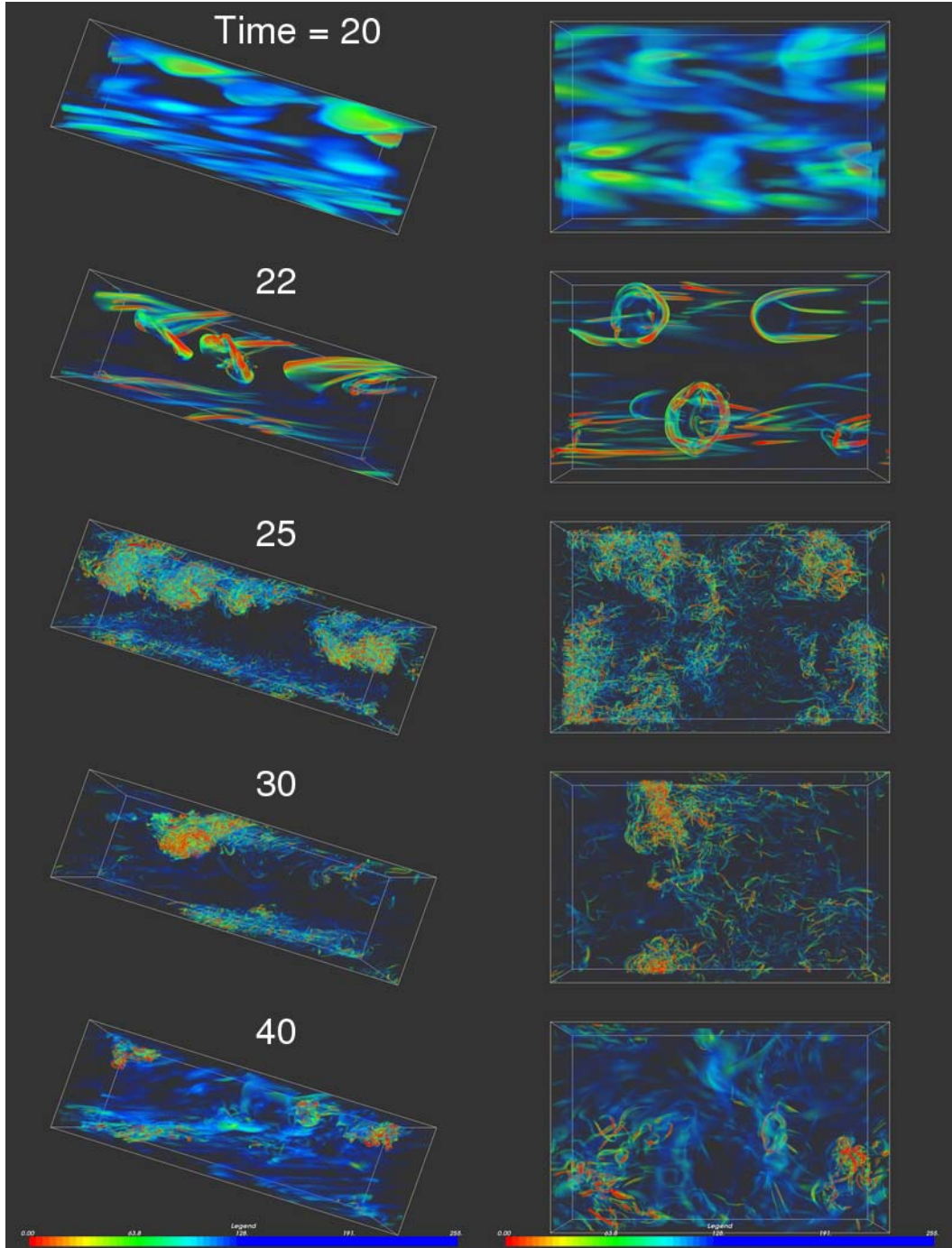


Figure 18. 3D evolution of vortex tubes (λ_2 visualization) for an amplitude $A=0.9$ gravity wave viewed from the side and from above. Red and yellow regions denote the most intense rotation. Wave propagation is to the left in all panels.

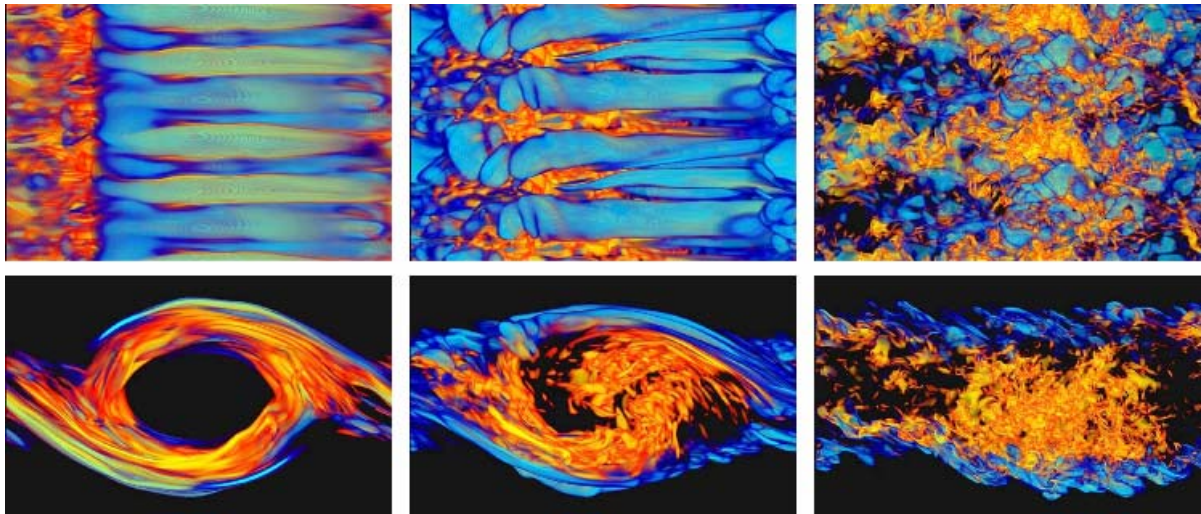


Figure 19. 3D volume rendering of the thermal (blue) and viscous (orange) dissipation for a wind-shear simulation with $Ri=0.05$. The top row shows the view from above at three distinct times. The bottom row shows the view from the side.

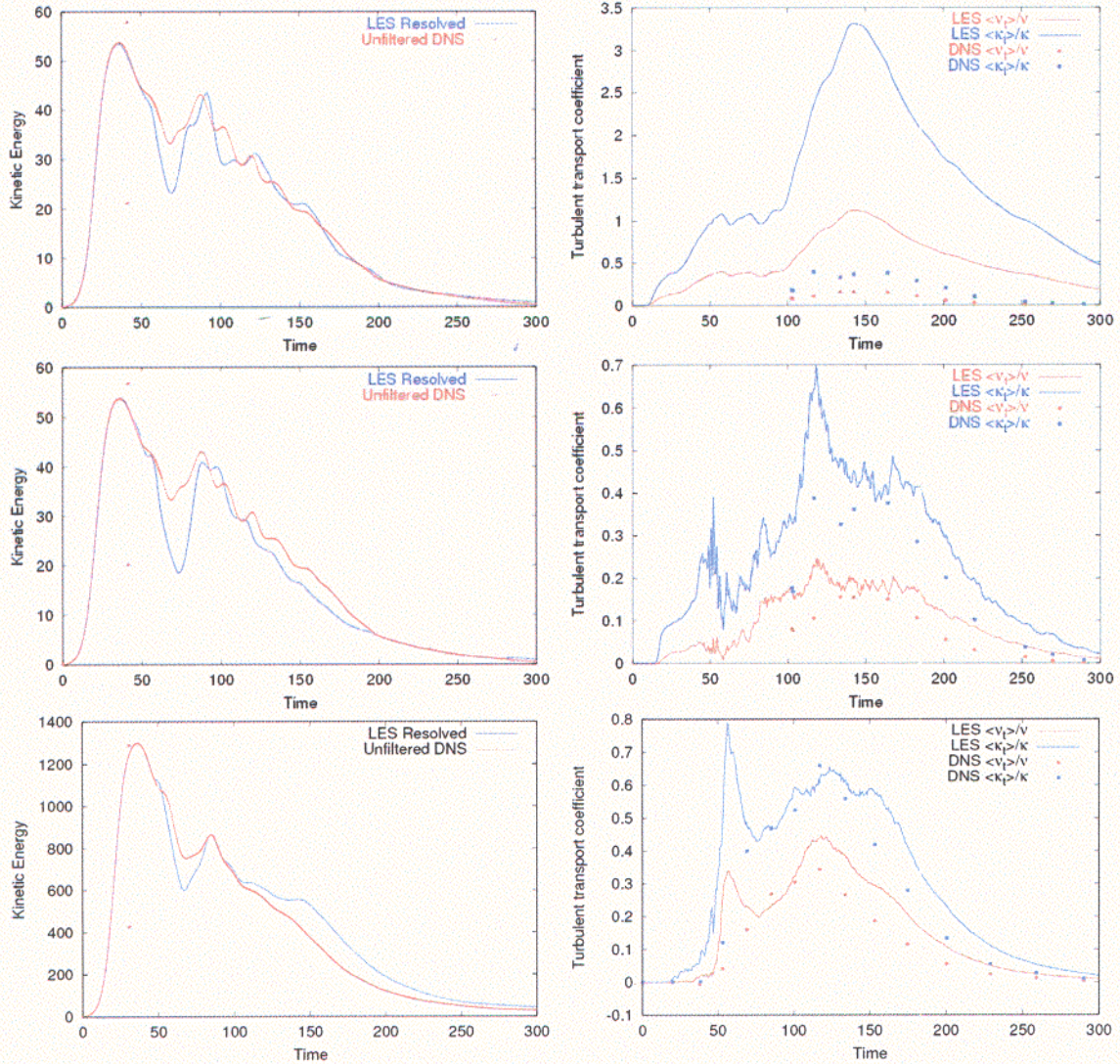


Figure 20. DNS/LES comparisons of wind-shear simulations with $Ri=0.05$ and $Re=2500$. Left panels show KE for LES (blue) and DNS (red). Right panels show eddy viscosity (red) and eddy diffusivity (blue) for the LES (solid line) and DNS (data symbols) solutions. Eddy quantities are evaluated from the DNS by first filtering to the LES resolution, and then computing the SGS quantities directly from the sub-filter fields. The top row shows results for an LES with a TKE SGS model, while the middle and bottom panels show results for a dynamic-Smagorinsky model. The top and middle rows show results for DNS and LES on small domains of size $(\lambda, \lambda/3, 2\lambda)$ using up to $(800, 270, 1600)$ spectral modes for the DNS and $(120, 40, 240)$ grid points for the LES, while the bottom row shows results on a large domain of size $(4\lambda, 2\lambda, 2\lambda)$ with up to $(3000, 1500, 1500)$ modes for the DNS and $(480, 240, 240)$ modes with the LES.

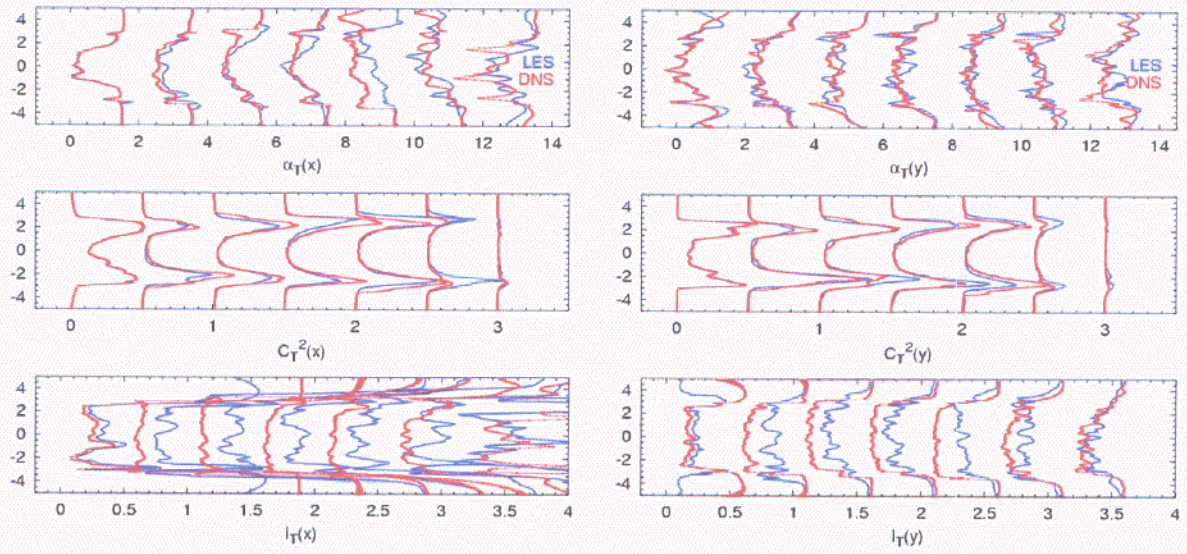


Figure 21. Structure-function-fit parameters versus height for LES (blue) and DNS (red) solutions. Structure functions are computed separately for streamwise (x) and spanwise (y) spatial separations. The two solutions are statistically indistinguishable, demonstrating that the LES is able to reproduce the DNS results while using 1300 times less computer time. See *Werne & Fritts 2000* for details on the computation of the 2nd-order structure-function-fit parameters.

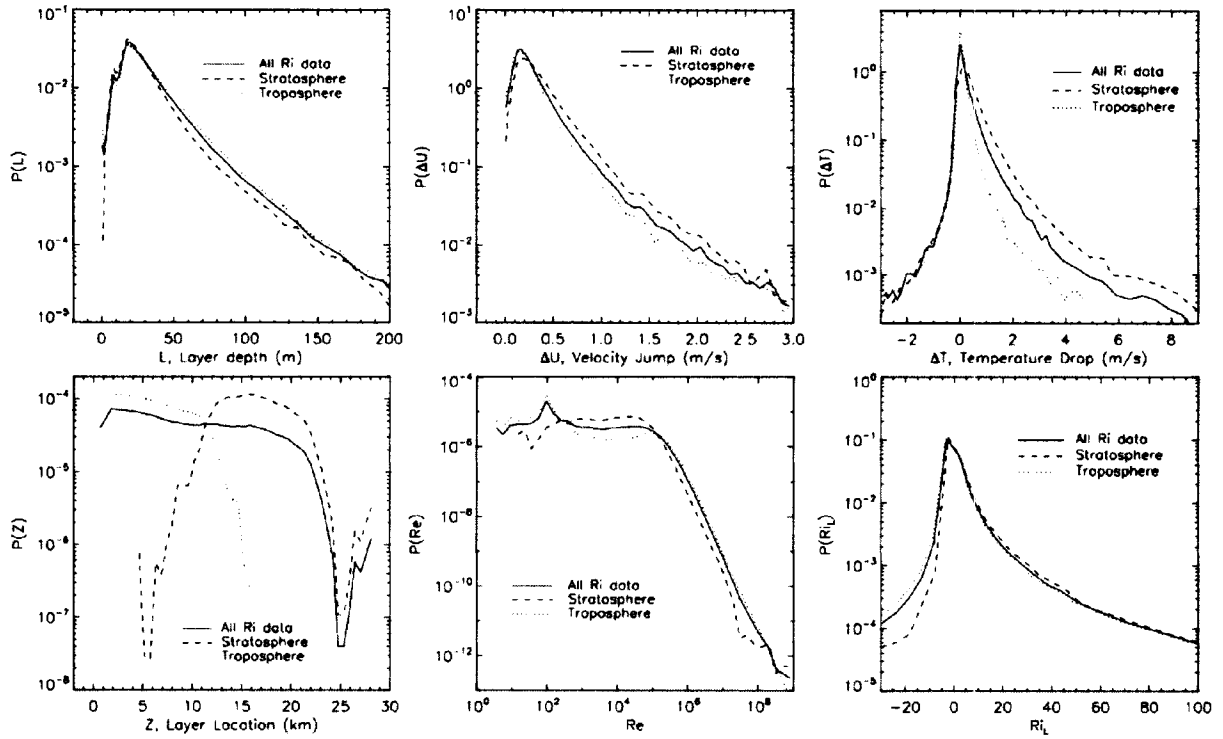


Figure 22. Probability density functions for atmospheric shear layers derived from 440 rawinsonde flights over Kansas and Utah. Top row from left to right: L , layer depth; ΔU , velocity jump across layer; ΔT , temperature drop across layer. Bottom row from left to right: Z , layer height; $Re = \Delta U L / \nu$, layer Reynolds number; $Ri_L = g \alpha \Delta T / (\Delta U)^2$, layer bulk Richardson number. All panels contain three curves. The dashed (dotted) curve is for raw data located above (below) the tropopause. The solid curve results from all the data.

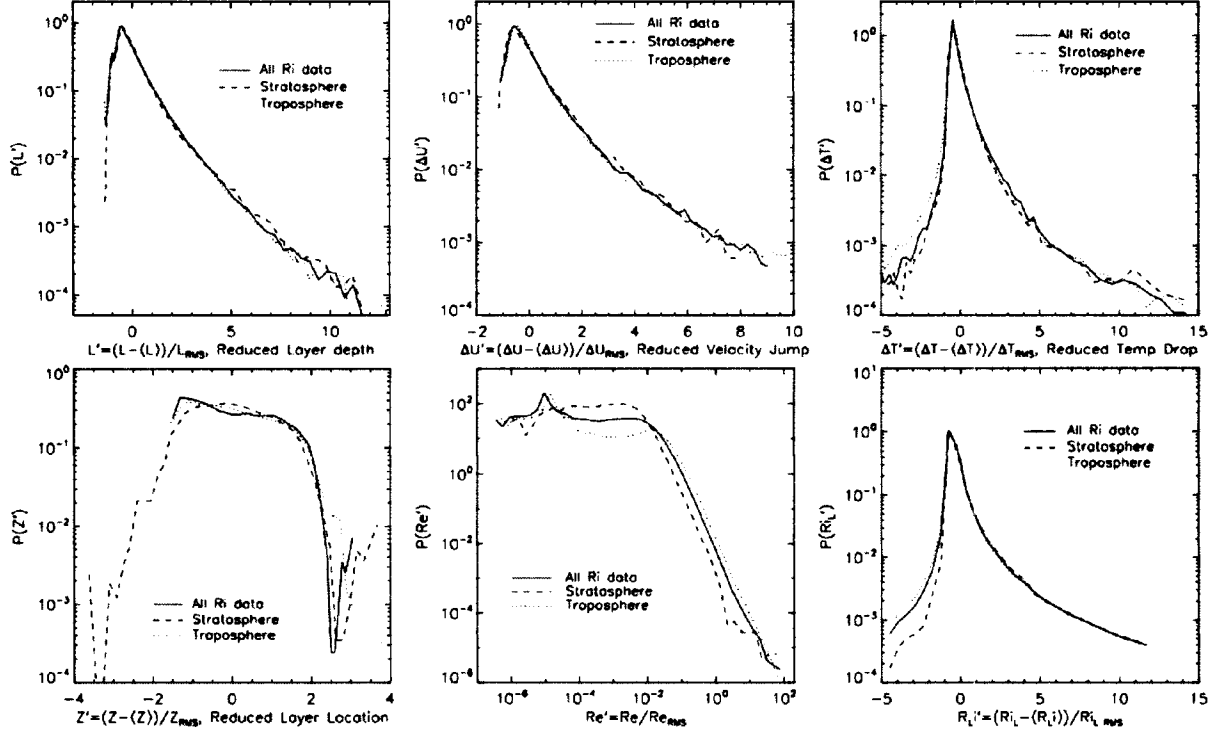


Figure 23. Same as Figure 22, but all PDFs are with respect to the reduced variables $X' = (X - \langle X \rangle) / X_{RMS}$, where X represents one of the variables plotted in Figure 22, and $\langle X \rangle$ and X_{RMS} are the average and RMS values of X respectively. If the PDF versus the reduced variable X' is identical in the troposphere and stratosphere, then it possesses a universal form and can be easily represented by $\langle X \rangle$ and X_{RMS} .

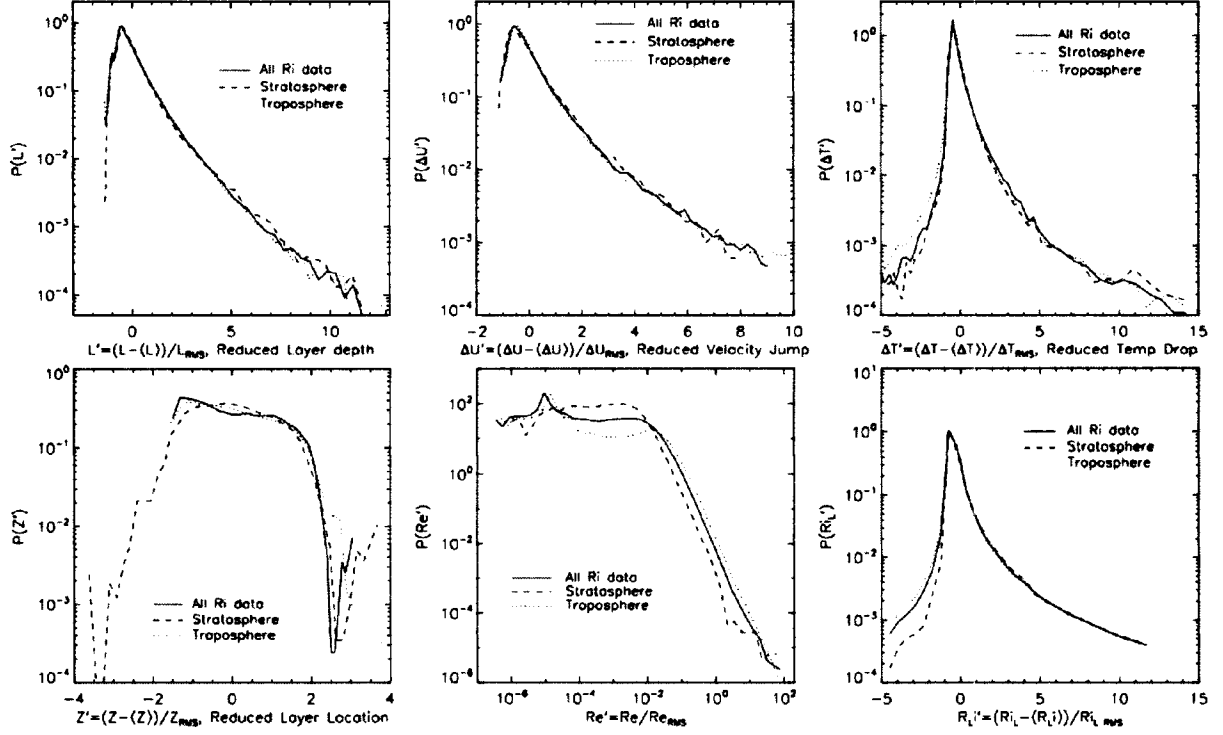


Figure 23. Same as Figure 22, but all PDFs are with respect to the reduced variables $X' = (X - \langle X \rangle) / X_{RMS}$, where X represents one of the variables plotted in Figure 22, and $\langle X \rangle$ and X_{RMS} are the average and RMS values of X respectively. If the PDF versus the reduced variable X' is identical in the troposphere and stratosphere, then it possesses a universal form and can be easily represented by $\langle X \rangle$ and X_{RMS} .

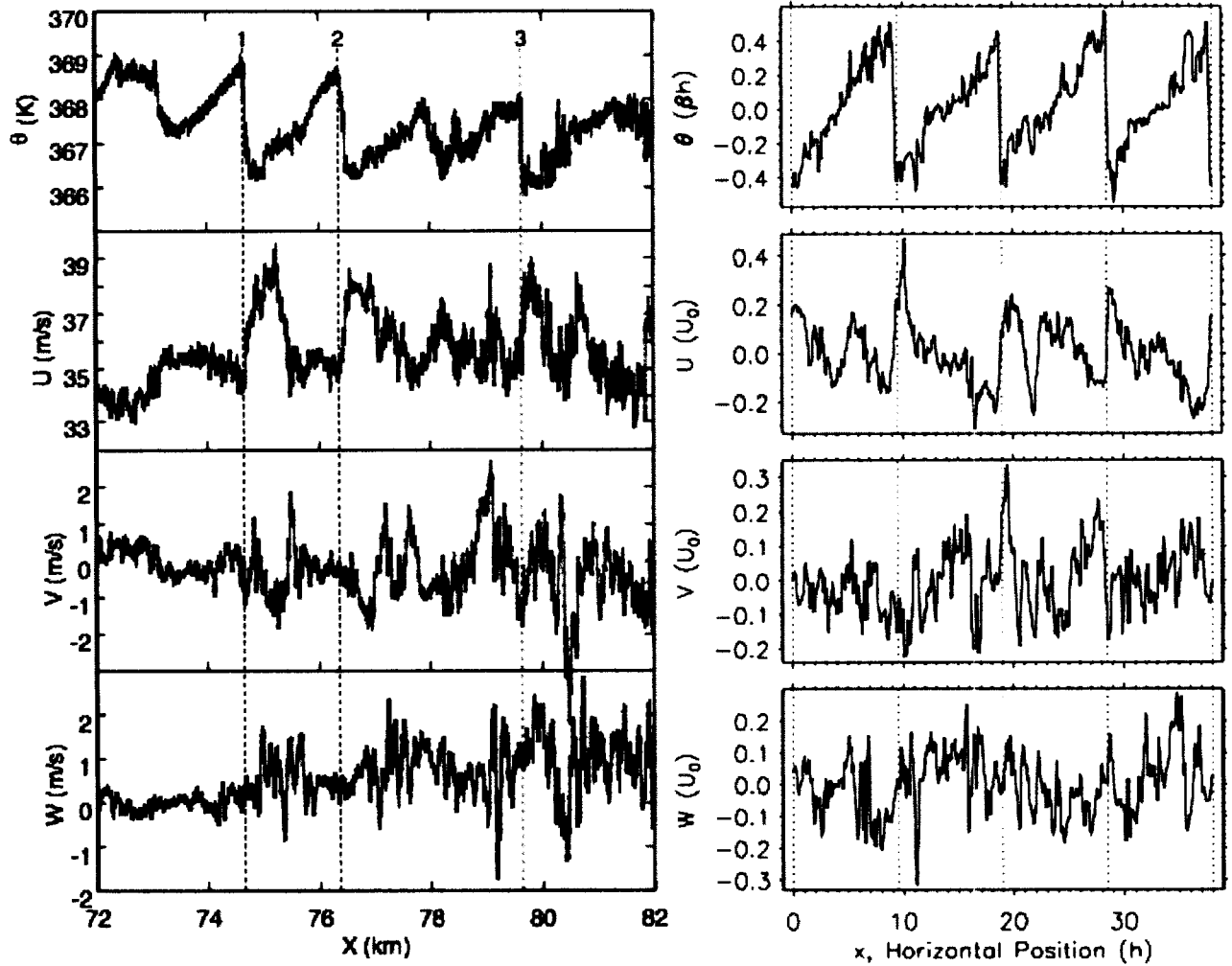


Figure 24. *Cliff-ramp structures in aircraft measurements (left) and DNS wind-shear solutions (right). The left panel shows four time traces (from top to bottom) for aircraft-measured potential temperature θ , streamwise velocity U , spanwise velocity V , and vertical velocity W along a streamwise flight track over Wales at an altitude of 11.4 km. The data were collected using Airborne Research Australia's Grob G520T Egrett outfitted with three NOAA BAT probes positioned under each wing and high on the tail (see Wroblewski et al, 2003). Similar structures are observed along paths through the DNS at $Ri=0.15$ and $Ri=0.20$. The right panels show such structures at $t=77 h/U_0$. See text for more discussion of the data and comparisons between the DNS and aircraft data.*

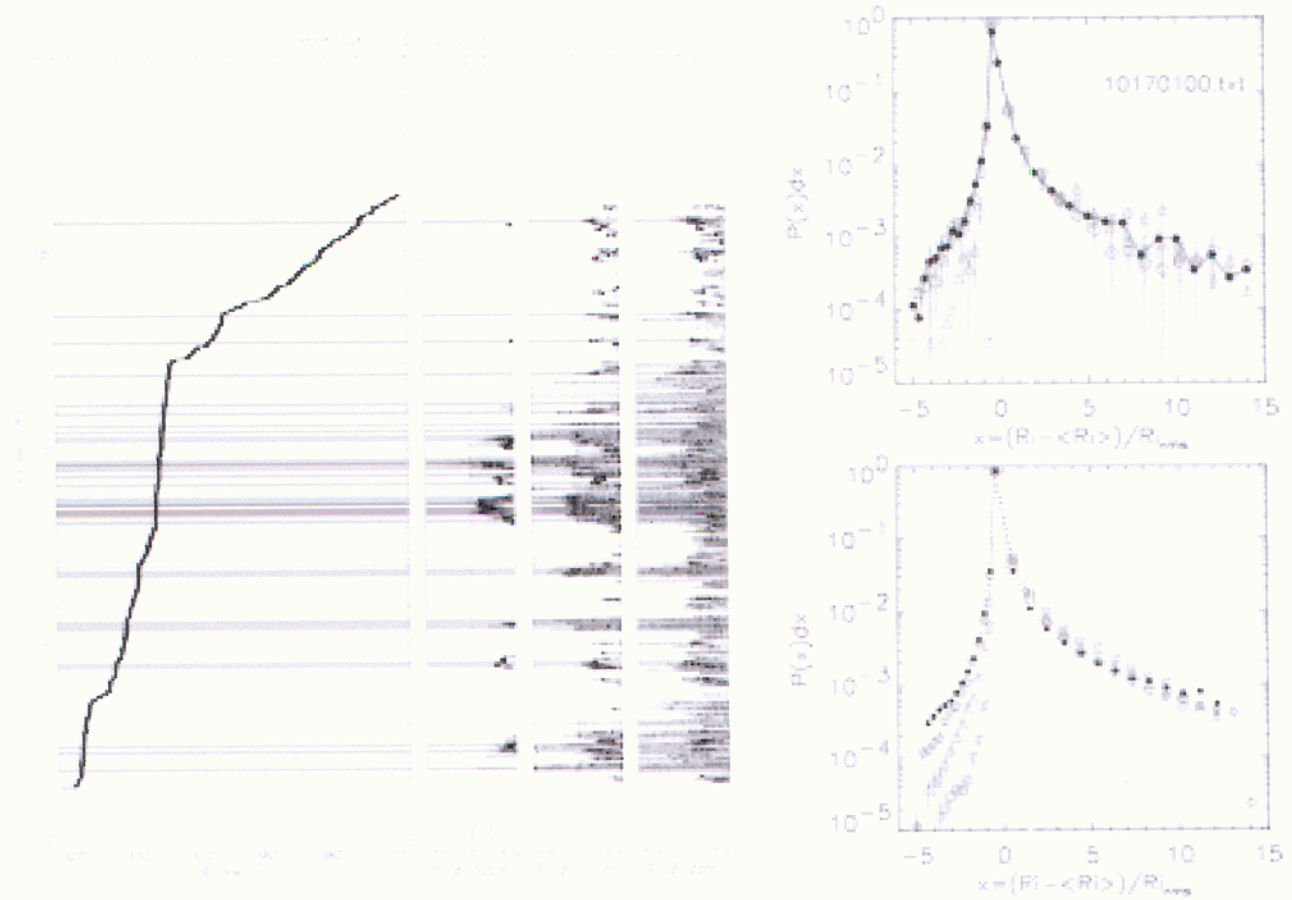


Figure 25. *Left panel: VTMX Wheeler Farm rawinsonde data, 17 Oct 2000, 0:48 UTC. Left-most sub-panel shows raw potential temperature $\theta(z)$. $Ri_\delta(z)$ is plotted on right for three different data filters: $\delta=33m$, $101m$, and $300m$. $Ri_\delta(z)$ is computed after applying filter to $\theta(z)$ and winds. Regions with $Ri < 0.25$ are shaded gray, with the shading level determined by the value of the largest filter scale for which $Ri < 0.25$ is satisfied. Upper-right panel: Probability Density Functions (PDFs) of $Ri_\delta(z)$ data from the left panel. Solid symbols: 11m-smoothed data. Open circles: 33m smoothing. Triangles: 101m smoothing. Squares: 300m smoothing. Lower-right panel: Ensemble PDFs for all Wheeler Farm data collected at VTMX. Note the reduced error bars and better-defined functional dependence on δ for the ensemble data.*

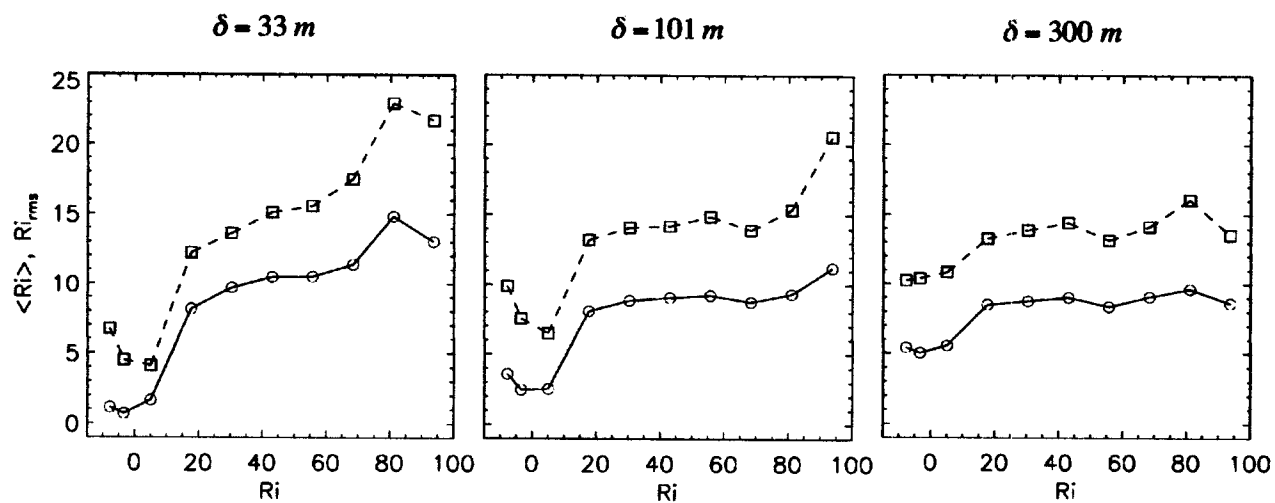


Figure 26. Mean and RMS of the ensemble PDF's shown in Figure 25.

REFERENCES

- Beland, R.R., 1993: Propagation through atmospheric optical turbulence. In F.G. Smith, editor, *The Infrared and Electro-Optical Systems Handbook*, Vol. 2, pp. 157-232. SPIE Engineering Press.
- Bernardo, J.M. and A.F.M. Smith, 1994: *Bayesian Theory*. John Wiley & Sons, New York.
- Berliner, L.M., 2003: Physical-statistical modeling in geophysics. *J. Geophys. Res.*, **108**(D24):8776, doi: 10.1029/2002JD002865.
- Berliner, L.M., R.F. Milliff and C.K. Winkle, 2003: Uncertainty and climate change. *J. Geophys. Res.*, **108**(C4):3104, doi:10.1029/2002JC001413.
- Bolgiano, R. 1959: Turbulent Spectra in a Stably Stratified Atmosphere, *J. Geophys. Res.*, **64**, 2226-2229.
- Coulman, C.E., J. Vernin, and A. Fuchs, 1995: Optical seeing: Mechanism of formation of thin turbulent laminae in the atmosphere. *Applied Optics*, **34**, 5161-5474.
- Dewan, E.M., 1980: Optical Turbulence Forecasting: A Tutorial. Air Force Geophysics Laboratory Technical Report, AFGL-TR-80-0030, ADA 086863.
- Dewan, E.M., R.E. Good, R. Beland, and J. Brown, 1993: A Model for C_n^2 (Optical Turbulence) Profiles Using Radiosonde Data. Phillips Laboratory Technical Report 93-2043, ADA 279399.
- Dunkerton, T.J., 1989: Theory of internal gravity wave saturation. *Pure Appl. Geophys.* **130**, 373-397.
- Fritts, D.C., C. Bizon, J. Werne, and C.K. Meyer, 2003: Layering accompanying turbulence generation due to shear instability and gravity wave breaking. *J. Geophys. Res.*, **108**, D8, 8452, doi:10.1029/2002JD002406.
- Fritts, D.C., S.L. Vadas, K. Wan, and J. Werne, 2006: Mean and variable forcing of the middle atmosphere by gravity waves, *J. Atmos. Solar-Terres. Phys.*, **68**, 247-265.
- Fritts, D.C., L. Wang, J. Werne, T. Lund, and K. Wan, 2007: Gravity wave instability dynamics at high Reynolds numbers, 1: Wave field evolution at large amplitudes and high frequencies, *J. Atmos. Sci.*, to be submitted.
- Germano, M., U. Piomelli, P. Moin, and W.H. Cabot, 1991: A dynamic subgrid-scale eddy viscosity model. *Phys. Fluids A*, **3**, 1760-1765.
- Gibson, 1962: Spectra of turbulence at high Re, *Nature*, **195**, 1281-1283.
- Gibson, 1963: Spectra of turbulence in a round jet, *J. Fluid Mech.* **15**, 161-173.
- Gibson-Wilde, D., J. Werne, D.C. Fritts, and R.J. Hill, 2000: Direct numerical simulation of VHF radar measurements of turbulence in the mesosphere. *Radio Sci.*, **35**, 783.
- Gurvich, A.S., and S.L. Zubkovskii, 1966: Estimate of the structure function of temperature fluctuation in the atmosphere, *Izv. Akad. Nauk SSSR, Fiz. Atmosf. I Okeana*, **2**, 202-204.

- Hill, R.J. and S.F. Clifford, 1978: Modified spectrum of atmospheric temperature fluctuations and its applications to optical propagation. *J. Opt. Soc. Am.*, **68**, 892.
- Jackson, A., 2004: Modified-Dewan Optical Turbulence Parameterizations. Air Force Research Laboratory Technical Report, AFRL-VS-TR-2004-1116, ADA 432901.
- Kaimal, J.C., J.C. Wyngaard, Y. Izumi and O.R. Cote, 1972: Spectral characteristics of surface layer turbulence, *Q. J. Roy. Meteor. Soc.*, **98**, 305-317.
- Kleisser, L. and U. Schumann, 1980: Treatment of incompressibility and boundary conditions in 3-D numerical spectral simulations of plane channel flows. In E.H. Hirschel, editor, *Proceedings of the 3rd GAMM Conference on Numerical Methods in Fluid Mechanics*, Vieweg, Braunschweig.
- Lombard, P.N. and J.J. Riley, 1996: Instability and breakdown of internal gravity waves, I. Linear stability analysis. *Phys. Fluids*, **8**, 3271-3287.
- Paquin, J.E., and S. Pond, 1971: The determination of the Kolmogorov constants for velocity, temperature and humidity fluctuations from second- and third-order structure functions. *J. Fluid Mech.* **50**, 257-269.
- Pettersson-Reif, B.A., J. Werne, Ø. Andreassen, C. Meyer, and M. Davis-Mansour, 2002: Entrainment-zone restratification and flow structures in stratified shear turbulence. In P. Bradshaw, editor, *Studying Turbulence Using Numerical Simulation Databases – IX, Proceedings of the 2002 Summer Program*, pp 245-256. Center for Turb. Res.
- Smagorinsky, J., 1963: General circulation experiments with the primitive equations. *Monthly Weather Review*, **91**, 99-164.
- Spalart, P.R., R.D. Moser and M.M. Rogers, 1991: Spectral methods for the Navier-Stokes equations with one infinite and two periodic directions, *J. Comput. Phys.*, **96**, 297-324.
- Sullivan, P.P., J.C. McWilliams and C.-H. Moeng, 1994: A subgrid-scale model for large-eddy simulation of planetary boundary-layer flows. *Boundary Layer Meteor.* **72**, 247-276.
- Sullivan, P.P., J.C. McWilliams and C.-H. Moeng, 1996: A grid nesting method for large-eddy simulation of planetary boundary-layer flows. *Boundary Layer Meteor.*, **80**, 167-202.
- Tatarski, V.I. 1961: *Wave Propagation in a Turbulent Medium*. McGraw-Hill, N.Y.
- Werne, J., 1995: Incompressibility and no-slip boundaries in the Chebyshev-Tau approximation: Correction to Kleiser and Schumann's influence-matrix solution. *J. Comput. Phys.*, **120**, 260-265.
- Werne, J., 1998: Letter to the Editor - Comment on 'There is no error in the Kleiser-Schumann influence matrix method', *J. Comput. Phys.*, **141**, 88-89.
- Werne, J., P. Adams and D. Sanders, 2000: Hierarchical Data Structuring: an MPP I/O How-to. *Scientific Computing at NPACI*, June 14, Vol. 4, issue 12.

- Werne, J. and D.C. Fritts, 2000: Structure Functions in Stratified Shear Turbulence. In Proceedings of the 2000 DoD User Group Conference, Albuquerque, NM.
- Werne, J. and D.C. Fritts, 2001: Anisotropy in a stratified shear layer. *Phys. Chem. Earth*, **26**, 263.
- Werne, J., T. Lund, B.A. Pettersson-Reif, P. Sullivan, and D.C. Fritts, 2005: CAP Phase II simulations for the Air Force HEL-JTO project: Atmospheric turbulence simulations on NAVO's 3000-PE IBM P4+ and ARL's 2000-PE Intel Xeon EM64T cluster. In *15th DoD High Performance Computing User Group Conf.*, Nashville, TN, June, 2005.
- Wroblewski, D., 2007: private communication.
- Wroblewski, D., O.R. Cote, J. Hacker, T.L. Crawford, and R.J. Dobosy, 2003: Refractive turbulence in the upper troposphere and lower stratosphere: analysis of aircraft measurements using structure functions. In *12th Symposium on Meteorological Observations and Instrumentation*, Long Beach, CA, Feb 2003.
- Wyngaard, J.C. and O.R. Cote, 1971: The budgets of turbulent kinetic energy and temperature variance in the atmosphere surface layer. *J. Atmos. Sci.*, **28**, 190-201.
- Wyngaard, J.C. and Y.H. Pao, 1971: Some measurements of the fine structure of large Reynolds number turbulence. In *Statistical Models and Turbulence, Proceedings of the Symposium at San Diego, July 15-21*, ed. M. Rosenblatt and C.V. Atta. Lecture Notes in Physics, Springer-Verlag, Berlin-Heidelberg, New York.

